


2011

Measurements in Air-water Bubbly Flow Through a Vertical Narrow High-aspect Ratio Channel

Benjamin R. Patrick
University of Central Florida

 Part of the [Mechanical Engineering Commons](#)
Find similar works at: <https://stars.library.ucf.edu/etd>
University of Central Florida Libraries <http://library.ucf.edu>

This Masters Thesis (Open Access) is brought to you for free and open access by STARS. It has been accepted for inclusion in Electronic Theses and Dissertations by an authorized administrator of STARS. For more information, please contact STARS@ucf.edu.

STARS Citation

Patrick, Benjamin R., "Measurements in Air-water Bubbly Flow Through a Vertical Narrow High-aspect Ratio Channel" (2011). *Electronic Theses and Dissertations*. 6659.
<https://stars.library.ucf.edu/etd/6659>

MEASUREMENTS IN AIR-WATER BUBBLY FLOW THROUGH A VERTICAL NARROW HIGH-ASPECT RATIO CHANNEL

by

BENJAMIN R PATRICK
B.S.M.E. University of Central Florida, 2008

A thesis submitted in partial fulfillment of the requirements
for the degree of Master in Science in Mechanical Engineering
in the department of Mechanical, Materials and Aerospace Engineering
in the College of Engineering and Computer Science
at the University of Central Florida
Orlando, Florida

Summer Term
2011

© 2011 Benjamin R. Patrick

ABSTRACT

Two-Phase bubbly flows are encountered in a wide range of industrial applications, particularly where phase changes occur as seen in high performance heat exchangers and boiling reactors for power generation. These flows have been extensively studied in channels with circular geometries using air-water flows, though little data exists for flows through narrow rectangular channels. Measurements in thin geometries are particularly challenging since large bubbles bridge the gap, and it is difficult to compare point measurements with photographic techniques. The objective of this study is to explore the abilities of hot-film anemometry and high speed photography for taking measurements in a narrow vertical rectangular channel for a range of volume fractions, with particular attention on the narrow dimension.

Hot-film anemometry (HFA) is a measurement technique originally developed for the measurement of fluid velocities, but has since been found to have applications for broader measurements in multiphase flow. With the sensor operating on the principle of heat loss, the method takes advantage of the differing abilities of the phases to transport heat, with each phase leaving its own signature in the signal response. The linchpin of this method lies in the ability to accurately distinguish between the two phases within the signal, and to execute this operation, various algorithms and techniques have been developed and used with some success for a wide range of flow conditions. This thesis is a study of the various methods of analysis such as amplitude threshold for triggering, and small slope threshold for finely tuning the edges of the bubble interactions, and demonstrates the capabilities of the hot-film sensor in a narrow rectangular vertical duct with a high aspect ratio.

A vertical acrylic test section was fabricated for the purposes of this study, inset with a rectangular channel 38.1mm in width and 3.125mm in depth. Experiments were conducted for volume fractions ranging from 2% to 35%, which remained within the limits of the bubbly flow regime, but ranged from small uniform bubbles to larger bubbles coalescing into a transition regime.

The hot-film signal was analyzed for void fraction, bubble speed, and bubble size. An in-depth study of the various methods of phase discrimination was performed and the effect of threshold selection was examined. High-speed video footage was taken in conjunction with the anemometer data for a detailed comparison between methods. The bubble speed was found to be in close agreement between the HFA and high-speed video, staying within 10% for volume fractions above 10%, but still remaining under a 30% difference for even as low as the 2% volume fraction, where measurements have been found to be historically difficult. The trends with volume fraction between the HFA and high-speed results were very similar. A correlation for narrow rectangular channels employing a simple drift flux model was found to compare with the void fraction data where appropriate. Good agreement was found between the methods using a hybrid phase discrimination technique for the HFA data for the void fraction and bubble speed results, with the high-speed video results showing a slight over-estimation in regards to the bubble size.

TABLE OF CONTENTS

LIST OF FIGURES	vii
LIST OF TABLES	x
CHAPTER ONE: INTRODUCTION.....	1
CHAPTER TWO: LITERATURE REVIEW	5
Air-Water Flow in Vertical Rectangular Channels.....	5
Hot-Film Anemometer Signal Response in Multiphase Flow	7
Hot-Film Anemometer Signal Analysis.....	11
CHAPTER THREE: METHODOLOGY	13
Experimental Facility	13
Air-Water Test Loop Overview	13
Vertical Test Section.....	14
Transverse Mechanism	15
Hot-Film Anemometer Data Acquisition System.....	18
High Speed Camera	19
HFA Signal Analysis	20
Phase Discrimination and Void Fraction	20
Void Fraction	21
Bubble Speed	22
Bubble Size	23
High Speed Camera Image Analysis	23

CHAPTER FOUR: RESULTS AND DISCUSSION	26
Cases Run.....	26
Comparison of Phase Discrimination Methods	29
Void Fraction	40
Bubble Speed	44
Bubble Size	47
CHAPTER FIVE: CONCLUSIONS	51
APPENDIX A: LOCATING CHANNEL CENTER.....	53
APPENDIX B: ERROR PROPOGATION AND UNCERTAINTY	56
APPENDIX C: HFA SIGNAL ANALYSIS CODE.....	60
Pure Slope Phase Discrimination and Void Fraction Calculation Code.....	61
Hybrid (Amplitude Trigger) Phase Discrimination and Void Fraction Calculation Code	62
Bubble Velocity Cross Correlation Code	64
Chord Length Distribution and Average Diameter Code	67
LIST OF REFERENCES	70

LIST OF FIGURES

Figure 1: Parallel Sensor Hot-Film Probe.....	2
Figure 2: Flow Regime and Transition Regimes for Vertical Narrow Rectangular Channels. (a) Bubbly, (b) Cap-Bubbly, (c) Slug, (d) Slug-Churn Transition, (e) Churn Turbulent, (f) Annular [6].....	5
Figure 3: Flow Regime Map and Transition Lines for a Narrow Rectangular Duct [12],[16].....	7
Figure 4: Typical Signal Response to Bubble Passage. A. Front interface, B. Rear interface, C. Detachment tail collapse, D. Return to liquid phase [18]	8
Figure 5: Probe Interfacial Meniscus Interactions. Left Front Interface, Right Rear Interface [19]	9
Figure 6: Non-Typical Bubble Signal Responses. (a) Vibrating Film, (b) Film Breakage, (c) Film Vibration then Break, (d) Two Consecutive Bubbles with Film Breaks [19]	10
Figure 7: Air-Water Test Loop Schematic.....	14
Figure 8: Vertical Test Section Diagram	15
Figure 9: Transverse Mechanism Schematic	16
Figure 10: Photograph of the Transverse Mechanism	17
Figure 11: Transverse Mechanism Exploded and Isometric Views	18
Figure 12: Image Processing Technique.....	24
Figure 13: Map of Superficial Liquid and Gas Velocities Examined.....	27
Figure 14: Sample Images from Volume Fraction of 2.2%	28
Figure 15: Sample Images from Volume Fraction of 15.2%	28

Figure 16: Sample Images from Volume Fraction of 35.3%	28
Figure 17: Sample of Hot Film Anemometer Signal Response - Amplitude	29
Figure 18: Sample of Hot Film Anemometer Signal Response – Slope.....	30
Figure 19: Amplitude Threshold Selection - Voltage Histogram.....	31
Figure 20: Amplitude Threshold Selection - Void Fraction vs. Threshold	32
Figure 21: Amplitude Threshold Selection – Derivative of Void Fraction vs. Threshold	32
Figure 22: Amplitude Threshold Selection - Chord Length vs. Threshold	33
Figure 23: Slope Threshold Selection - Void Fraction vs. Threshold	34
Figure 24: Slope Threshold Selection - Derivative of Void Fraction vs. Threshold	35
Figure 25: Slope Threshold Selection - Chord Length vs. Threshold	36
Figure 26: Threshold Selection Comparison - Void Fraction.....	38
Figure 27: Phase Discrimination Method and Threshold Selection Comparison.....	39
Figure 28: Channel Averaged Void Fraction Comparison	41
Figure 29: Sample Channel Width Void Fraction Profiles – High Speed Photography.....	42
Figure 30: Sample Channel Depth Void Fraction Profiles – HFA	42
Figure 31: Channel Center Void Fraction Comparison	43
Figure 32: Sample Channel Width Bubble Speed Profiles – High Speed Photography (Bars show one std. dev.).....	44
Figure 33: Sample Channel Depth Bubble Speed Profiles - HFA.....	45
Figure 34: Bubble Speed Comparison - Volume Fraction.....	46
Figure 35: Bubble Speed Comparison – Percent Difference between HFA and High Speed Photography	46

Figure 36: Sample Channel Width Bubble Size Profiles – High Speed Photography (Bars show one std. dev.)	47
Figure 37: Sample Channel Depth Bubble Size Profiles – HFA (Bars show one std. dev.)	48
Figure 38: Bubble Size Comparison - Volume Fraction	49
Figure 39: Bubble Size Comparison – Percent Difference	50
Figure 40: Channel Depth Tests Results.....	55

LIST OF TABLES

Table 1: Test Matrix.....	26
Table 2: Phase Discrimination Method and Threshold Selection Comparison	36
Table 3: HFA and Camera Uncertainty Analysis	57

CHAPTER ONE: INTRODUCTION

The study of two-phase flows has been largely conducted for medium to large vertical circular tubes, and has become a well established field, though large interest lies in flows through channels with alternative geometries. Narrow rectangular channels have presented themselves of particular interest for its industrial applications as well as for fundamental experimentation in the development of instrumentation and modeling [1],[2],[3],[4]. Industrial uses include heat exchangers in small electronics and machines where high-performance cooling is required in small spaces, as well as in power generation where the narrow rectangular geometries have applications in evaporator channels [5]. Unlike in larger channels, bubbles in narrow channels can quickly become large enough to bridge the gap between the walls, leading to entirely different flow effects and regimes than that seen in larger channels [6]. The flat walls of the channel lend themselves to the use of optical measurements such as gamma densitometry, laser Doppler velocimetry, and high speed video [7], [8], but this bridging of the gap effect leads to difficulty in interpreting the optical data for what occurs along the narrow dimension of the flow. For this purpose a hot-film anemometer has been paired with high-speed photography to examine both the wide and narrow dimension of flow, and to compare to each other where possible.

Hot-wire anemometry is a well established method for measuring flow properties in single phase systems. They are valued for their simplicity of use as well as minimal intrusiveness. Hot-film sensors consist of miniscule quartz tube coated by a thin-film of platinum, as opposed to a single thin wire. Though inherently fragile due to its size, hot-film

sensors are considered to be much more robust than their hot-wire counterparts, as the quartz provides extra rigidity, giving the slightly larger diameter. Typical sensor diameters for hot-wire probes range from .5 to 5 μm , and hot-film sensors range from 25 to 50 μm [9]. The probe acquired for this study is a TSI model 1244-20W parallel hot-film sensor probe, which has two sensors a known distance apart for the purpose of tracking the speed of flow effects, in this case bubble interfaces. This probe can be seen pictured below.

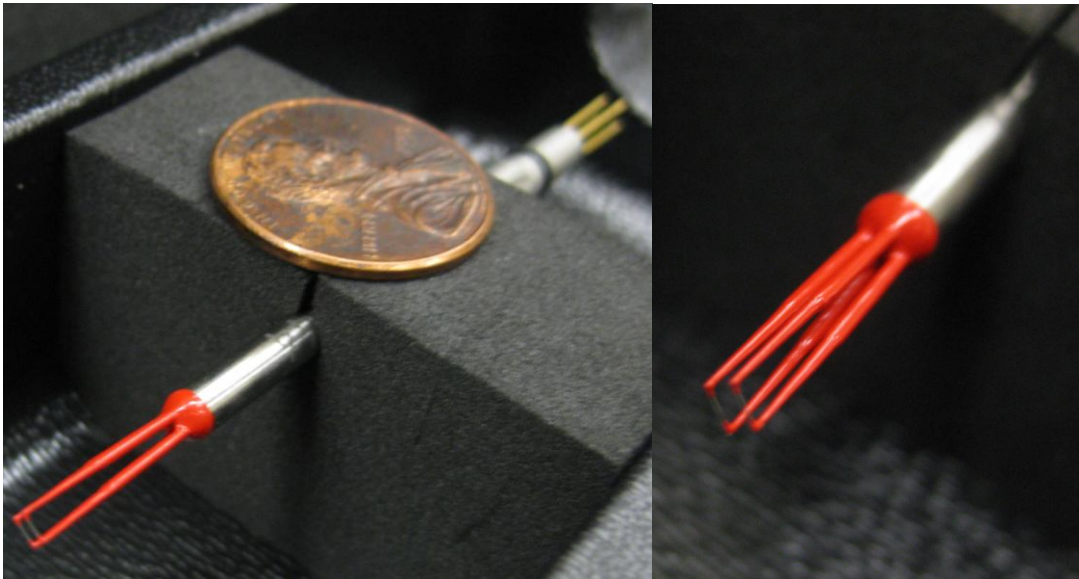


Figure 1: Parallel Sensor Hot-Film Probe

There are multiple ways of using these sensors to read the flow characteristics, all relying on the heat transfer capabilities of the flow of interest. The anemometer acquired for this project is what is known as a constant temperature anemometer (CTA), though in electrical terms it is considered to be held at a constant resistance. The resistance of highly conductive metals can be directly related to their temperature, thus by controlling the resistance of the sensor element, the temperature is also directly controlled. The IFA 300 uses a Wheatstone bridge electrical configuration to maintain the sensor at a constant resistance [10]. As convective heat losses to

the fluid increases, the amount of power supplied to the sensor must also increase to maintain the constant temperature/resistance. The power level is varied by an increasing and decreasing voltage across the sensor, and this voltage history is then in turn converted to a digital signal and recorded by a high-speed data acquisition system. The principle of usage in multiphase flow comes from the differences in thermal conductivity between two phases, each phase having distinct heat transfer properties. The phase with the higher thermal conductivity will cause higher heat losses and report higher voltages, alternatively the phase with the lower conductivity will absorb less heat, and report lower voltages. The crux of the analysis is differentiating between the two phases within the signal, and once this is done the flow properties are easily derived.

This study compares the various methods of phase discrimination of the HFA signal, using new techniques to take an in depth look at threshold selection for both amplitude and slope triggering. After finding satisfaction with a hybrid method of phase discrimination, and a threshold selection based on physical principles, the results were analyzed for void fraction, bubble speed, and bubble size. High-speed video was also taken, using MATLAB's very robust image processing capabilities to quickly and accurately analyze results. Results from center of the images could be compared with the HFA, being centered on the channel, with the full image being compared with a correlation formulated on the drift flux model for the entire channel.

The test section used for this study is oriented vertically with a rectangular channel 38.1mm in width and 3.125mm in depth. Flow straighteners at the entrance of the channel ensure a uniform flow before the bubbles are injected using a porous sparging stone, similar to that employed by [11]. The conditions for the experiments were well controlled and span across

the limits of the bubbly flow regime. Volume fractions studied range from as low as 2% to as high as 35%, reaching into cap-bubbly transition regime.

CHAPTER TWO: LITERATURE REVIEW

Air-Water Flow in Vertical Rectangular Channels

Mishima et al. [12] studied vertical narrow channels with gaps ranging from 1mm to 5mm using neutron radiography and high-speed video. Flow regime maps were generated from the high-speed video for channel gaps of 1.0mm, 2.4mm, and 5.0mm considering bubbly flow, slug flow, churn flow, and annular flow. The regime shapes and transitions were much different than that seen in circular tubes, even of smaller diameter, due to the crushing effect of the walls as was expected. The experimental results for slug-annular agreed well with the model developed by Jones and Zuber [13], though it was shown that churn turbulent flow was not observed for the channel gap of 1.0mm. They were also able to compare their void fraction results to the drift flux model, using a distribution parameter provided by Ishii [14] for rectangular channels, and found there to be good agreement.

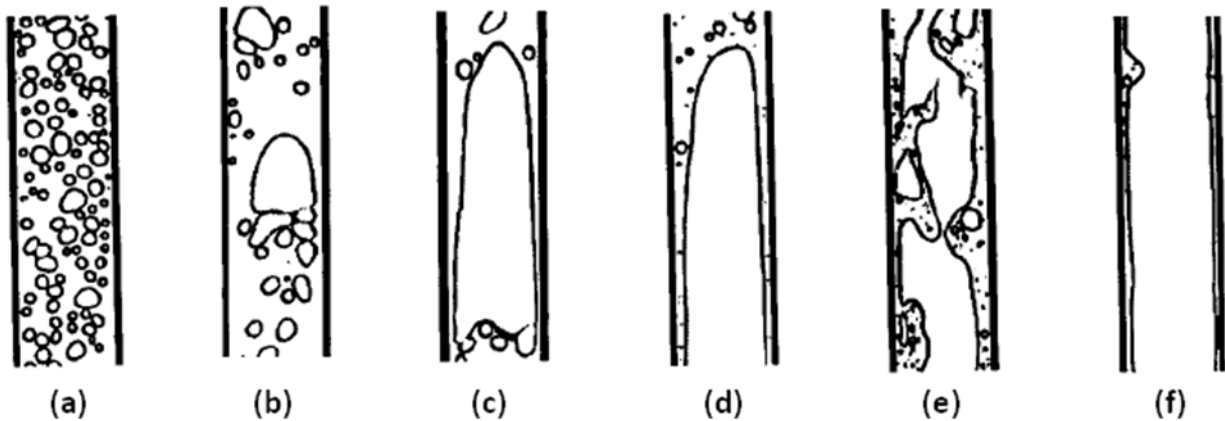


Figure 2: Flow Regime and Transition Regimes for Vertical Narrow Rectangular Channels. (a) Bubbly, (b) Cap-Bubbly, (c) Slug, (d) Slug-Churn Transition, (e) Churn Turbulent, (f) Annular [6]

Wilmarth and Ishii [6] extended this study to horizontal channels (gaps 1.0mm and 2.0mm), and identified transition regimes described as cap-bubbly, slug-churn transition, and churn-annular transition for the vertical channels. These regimes can be seen in Figure 2. The flow regime maps agreed well with those found by Mishima et al. [12], except for observing a churn turbulent regime for the 1.0mm gap that was reported to be missing by the previous study. Xu et al. [15] observed vertical channels for gaps 1.0mm and less (.6mm and .3mm), and showed that as the gap decreases the transition lines shift ‘left’, meaning the transitions occur at lower superficial gas velocities, due to increased wall friction and shear stress. Again, churn turbulent flow was observed for the 1.0mm channel (and smaller), and it was found that for the 0.3mm regular bubbly flow was not shown for even very low superficial gas velocities, staying in a cap-bubbly flow.

Hibiki and Mishima [16] developed models for flow regime transition for upward flow through narrow channels and compared with the existing data for gaps ranging from .3mm to 17mm. The regimes considered were bubbly flow, slug flow, churn flow, and annular flow. For bubble to slug, the transition occurred due to an increase in probability of bubble collisions, related to bubble size compared to the size of the channel gap and the void fraction. This occurred at a void fraction of 20% for bubbles larger than the narrow gap increasing up to 30% for bubbles much smaller than the gap, which is comparable to that of larger channels of both rectangular and circular cross section. The flow regime map for a gap size of 2.45mm from Mishima et al. [12] can be seen below with transition lines from Hibiki and Mishima [16] overlaid, showing good agreement between the model and experimental results.

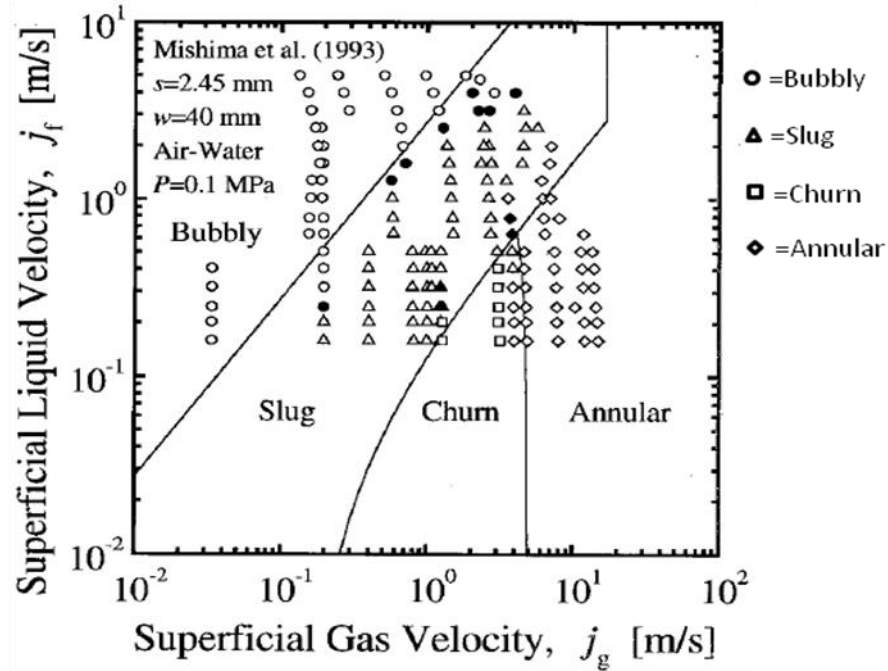


Figure 3: Flow Regime Map and Transition Lines for a Narrow Rectangular Duct [12],[16]

Hot-Film Anemometer Signal Response in Multiphase Flow

A constant temperature hot-film anemometer works on the principle of responding to differences in convection rates in a fluid flow. In single phase flows, this response is due to changes in velocity of the phase, with higher momentum fluid convecting away more heat, and requiring a higher power output to maintain the constant temperature. In multiphase applications, the principal cause of response is due to the difference in the heat capacities of the phases; however, any other causes of a convective difference in the flow will still be reflected in the signal. Typically, the footprints of alternative effects are small compared to the differences caused by the heat capacities, but they define the behavior in the transition zone surrounding the passage of a phase bubble. The signal response of the bubble interacting with the sensor has been studied in detail and is necessary in the understanding of the hot-film method.

A typical signal response to a bubble passage is characterized by a slight rise in the signal level as the bubble approaches, following a steep drop that smoothly approaches a low base level, a sharp upwards spike, and then a smooth transition back down to the regular signal level as the bubble drifts away. There is general agreement that the elevated signals preceding and following the bubble are caused by the motion of the liquid rapidly being displaced by the approaching volume. Bremhorst and Gilmore [17] studied the interaction at the phase interfaces using controlled dipping style tests, and concluded that the steep drop and smooth transition at the beginning was due to the exposure of the sensor to the gaseous phase, but with a thin liquid meniscus remaining attached to the sensor portion, which thins as the probe pierces further into the bubble. Further, they showed that the sharp spike at the end is due to a meniscus formation at the tail of the bubble, in which the interface holds onto the bubble causing a stretching effect. They concluded that the steep slope at the beginning of the interaction is to be included as a portion of the bubble phase, but the sharp spike at the end is a detachment tail and should not be included as portion of the natural bubble phase.

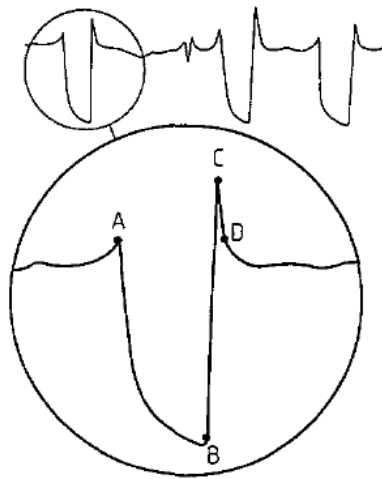


Figure 4: Typical Signal Response to Bubble Passage. A. Front interface, B. Rear interface, C. Detachment tail collapse, D. Return to liquid phase [18]

Faraar and Bruun [19] further studied the interactions that occurred at the interfacial barriers between the two phases, more closely examining the menisci that formed on the front and rear interfaces. It was shown that in a typical passage of the bubble, the rear interface intercepted the sensor before the meniscus from the front interface had detached, as shown in Figure 4 above. In certain instances, however, the front meniscus would collapse early, causing a spike midway through the bubble signal and in other cases when the two menisci met, the bubble would split into two halves. In all three of the cases, the film was shown to occasionally vibrate in a manner that gave a noisy signal within the bubble phase, and they concluded by cautioning against interpreting the various menisci effects as indication of multiple bubbles.

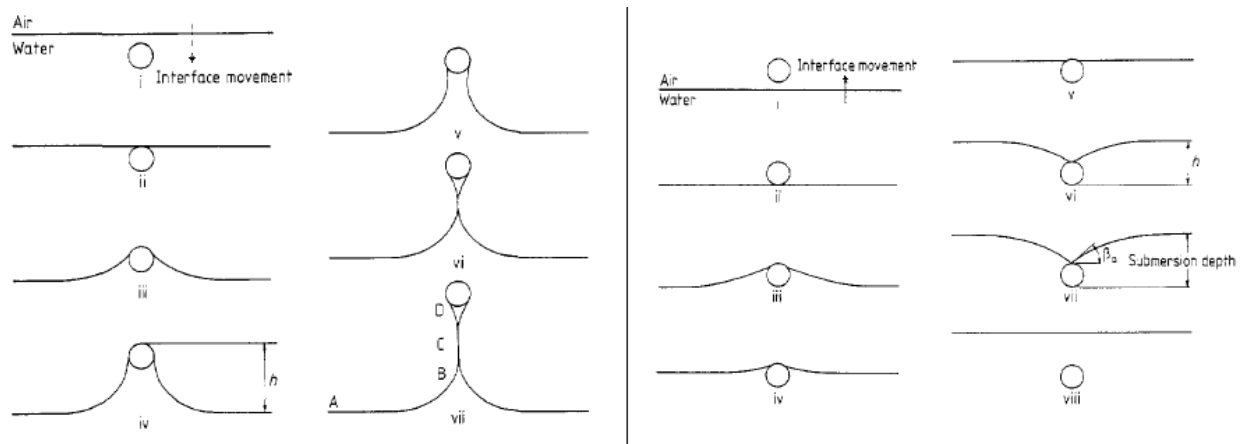


Figure 5: Probe Interfacial Meniscus Interactions. Left Front Interface, Right Rear Interface [19]

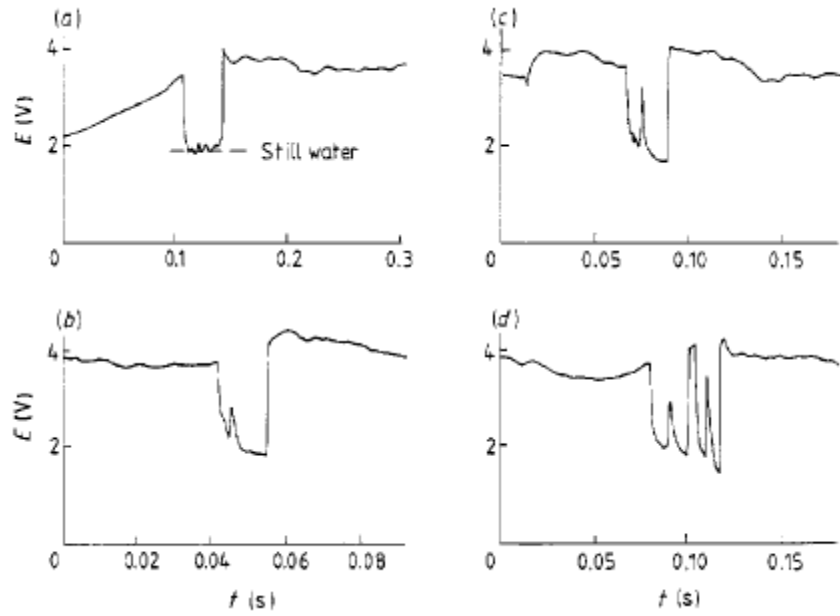


Figure 6: Non-Typical Bubble Signal Responses. (a) Vibrating Film, (b) Film Breakage, (c) Film Vibration then Break, (d) Two Consecutive Bubbles with Film Breaks [19]

Rensen [20] studied the effects of multiple types of bubble probe interactions, pointing out that instances of the bubble bouncing off of the sensor occurred in addition to the bubble being cleanly pierced or split into halves. Using a high-speed camera linked with a hot-film anemometer in a bubbly flow, they recorded the signal responses for each type of bubble interaction, in an attempt to find a pattern that would identify the type of interaction. Due to the variability of the bubble signal shapes, they concluded it was not possible to describe the type of interaction solely from the signal response. They noted that for bouncing and splitting bubbles the residence time was shorter, causing the bubbles to artificially appear smaller and thus could lead to low estimates of void fraction.

Hot-Film Anemometer Signal Analysis

To obtain useful information from the hot-film anemometer signal when applied to multiphase flow, it is necessary to be able to distinguish between the two phases. Toral [21] describes a method by which the amplitude of the signal is the basis of discrimination, denoting every voltage value above a threshold as the primary phase, and everything below it the secondary phase. To determine the voltage threshold a histogram of the voltage data is created, which reveals a bi-modal distribution. One peak refers to the most probable base voltage level of the primary phase, and other to the most probable base voltage level of the secondary phase, and a point between these two peaks is typically denoted as the threshold value. This specific point selected is up to the judgment of the researcher, and a few methods of selection are employed. Trabold et al. [22] recommends using the halfway point between the peaks, and Farrar et al. [18] recommends the lowest point between the two peaks. A study by Resch [23] recommends calculating the void fraction of the data for a range of threshold values, and then selecting the point at which the void fraction is least affected by changes in the threshold. In order to obtain a statistically significant histogram for threshold selection, a sampling time of 1 to 3 minutes is generally recommended [21].

Another prominent method of phase discrimination looks at the first-derivative of the signal, noticing that a sharp negative spike occurs with the passage of the liquid-gas interface, and that a sharp positive spike occurs with the passage of the gas-liquid interface. A slope-threshold is then denoted based on the difference in voltage amplitude of the two-phases, and the observed time it takes for the signal to fluctuate between the two voltage levels. When the derivative of the signal passes the negative threshold, the beginning of the gas phase is noted,

and the signal is considered gaseous until the derivative passes the positive threshold. This method was detailed by Farrar and Bruun [19]. Both of these basic methods have their advantages and disadvantages, and are appropriate in different situations, discussed in length by Farrar et al. [18].

Once the phases can be identified, it is useful to translate the data into a phase indication form, setting all values associated with the liquid phase as 1 and all values associated with the gaseous phase as 0. With this, various properties of the flow can be understood. The bubble frequency is found from the number of bubbles, indicated by the passing of two interfaces, experienced during the time of the experiment. For set ups employing two parallel sensors, bubble speed can be found by the time shift of the interfaces being recognized between the two signals, along with the known distance between the two sensors. With a known bubble speed, a bubble streamwise length can be found from the time duration of the probe/bubble interaction. These methods have been successfully described and employed with different details by [24] [25], [26], and [27]. The specific methods employed for the purposes of the present research will be discussed in further length in the Methodology section.

CHAPTER THREE: METHODOLOGY

Experimental Facility

Air-Water Test Loop Overview

An air-water test loop was created to maintain steady and controllable air and water flow rates in order to simulate various bubbly flow conditions in a vertical acrylic test section. A rotary vane type positive displacement pump ($\frac{1}{4}$ HP, 1725 RPM) pumps water from a reservoir through the entirety of the loop and back into its own reservoir. The flow rate is regulated by two flow control valves, redirecting portions of the water back into the water reservoir before entering the circuit. The liquid flow rate in the loop is measured by a 0-2 liters per minute infrared paddle wheel turbine type flow meter. The air is delivered by a piston style air pump (3.5 W, 60 Hz), and is injected into the vertical test section through a porous bubble stone. The air flow rate is controlled by a needle valve, and measured by a 0-.5 liter per minute hot mesh type air flow meter. A check valve is placed between the flow meter and the test section in order to prevent water from backing up into the air line and compromising the sensitive hot-mesh sensor. A thermocouple is placed in the line just before the loop dumps to the reservoir in order to monitor the temperature of the water just coming past the hot-film sensor. The liquid flow meter, air flow meter, and thermocouple data are read by modules on an NI cDAQ, recorded by a custom LabView VI, and then saved in spreadsheet format for future reference.

All piping in the system is semi-transparent $\frac{1}{4}$ " ID polyethylene tubing, other than the $\frac{1}{16}$ " vinyl air lines, and an 18" portion of $\frac{1}{4}$ " copper tubing leading up the liquid flow meter, in order to create a sufficiently developed flow for the flow meter to measure. A 2ft length of $\frac{1}{2}$ "

Schedule 80 transparent PVC is located just before the vertical test section, that allows for a viewing of the flow, namely to ensure that no extraneous air is entrained in the flow preceding the air input section. A mesh filter is placed before the control valves in order to collect any particles that enter the flow that could be hazardous to the liquid flow meter or hot-film anemometer probe. A schematic of the loop can be seen below in Figure 7.

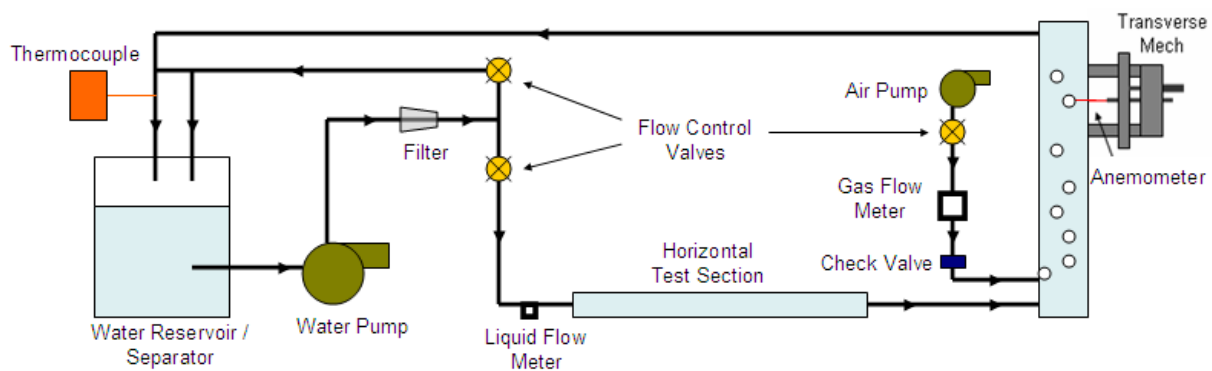


Figure 7: Air-Water Test Loop Schematic

Vertical Test Section

The vertical test section consists of three pieces of acrylic glass held together by a series of bolts. One section has the channel carved into it, along with the flow strengtheners at the entrance, a smaller center section piece has a rubber seal inset into a groove surrounding the channel, and the third section acts to sandwich the center section into the first section, creating the seal.

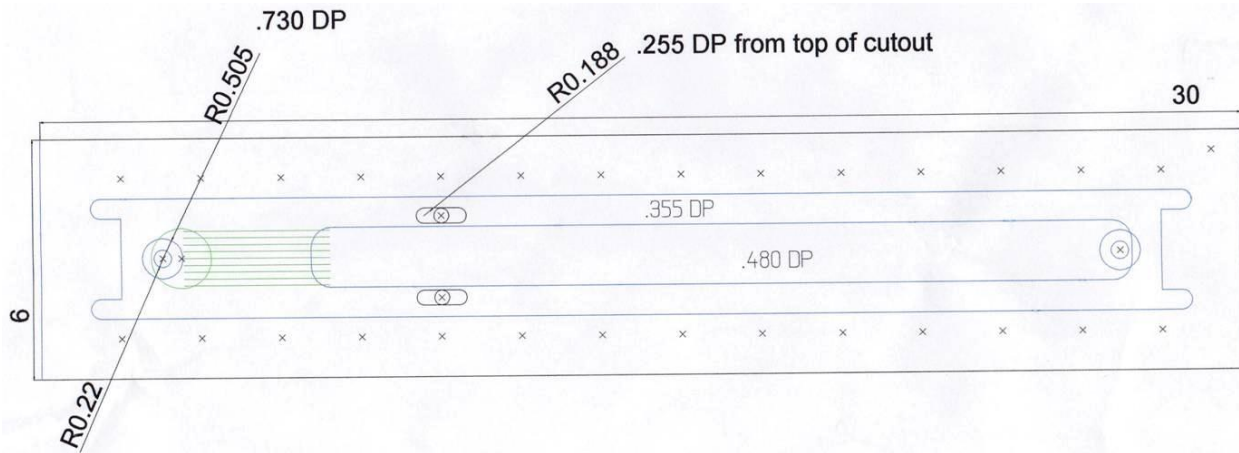


Figure 8: Vertical Test Section Diagram

Transverse Mechanism

The transverse mechanism uses a screw-type micrometer (.001" graduation) to control the position of the probe. The micrometer sleeve is locked into a four column frame that stiffly mounts to the face of the test section. The micrometer spindle is locked onto a plate that is able to freely slide along the support columns. The probe support is also locked to this sliding plate, thus is directly controlled by the micrometer. The probe rests inside of the probe support, and enters the section through an o-ring type connection fitting. The o-ring allows the section to maintain sealed while the probe is in motion, but causes a friction force that could cause the probe to become unseated from its support. A custom connection piece was created that grabs onto a lip of the probe and locks onto the support by a set screw, causing joint motion of the two pieces.

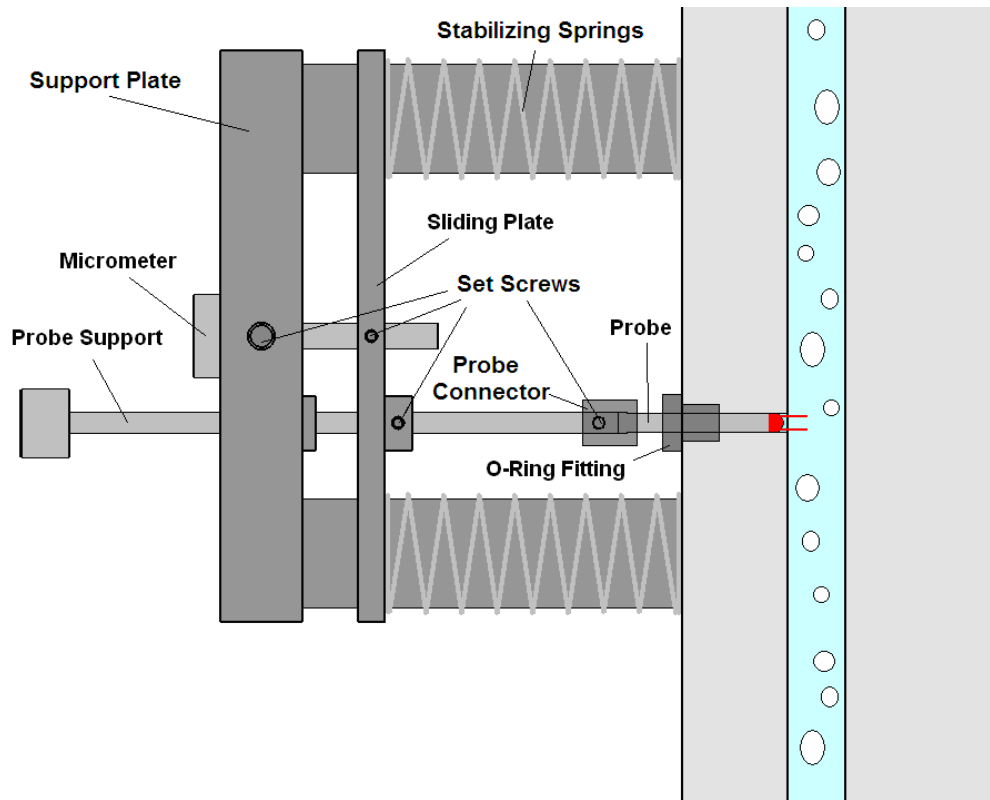


Figure 9: Transverse Mechanism Schematic

Any bending or twisting of the sliding plate would cause uncertainty in the location of the probe in respect to the micrometer, so a 90 degree angle must be constantly maintained between the plate and the support columns. To ensure the sliding plate remains strictly vertical, the columns and plate were very tightly toleranced, requiring pre-lubricated bushings in the guide holes to allow sliding to occur. Springs on each column maintain an even loading on the plate, as any slight twisting motion will cause it to lock in place, unable to move. The columns themselves rest inside counterbores on the support plate, rigidly maintaining themselves parallel in respect to one another. These various measures and connection pieces ensure a smooth direct one-to-one motion between the micrometer spindle and the probe sensor.

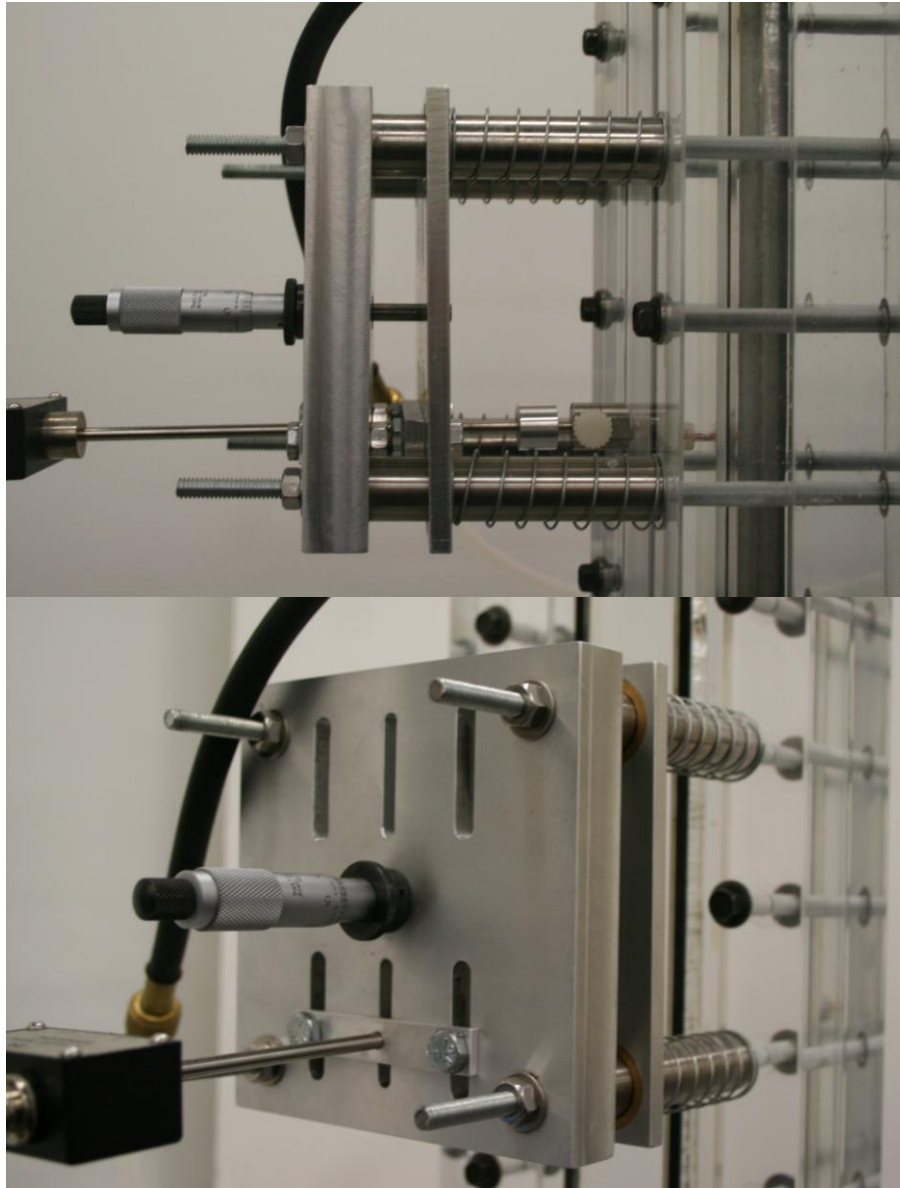


Figure 10: Photograph of the Transverse Mechanism

The mechanism was also designed to be flexible in its placement of the sensor. The four columns are spaced such that they attach onto any four bolt holes that span along the height of the test section. Further, grooves in the support plate and sliding plate allow the probe to be shifted up and down within the area between the four bolt holes. The combination between bolt hole selection and shifting of the probe allow the sensor to take measurements at any vertical

location in the test section where an o-ring fitting can be placed. Further views of the mechanism details can be seen in Figure 11.

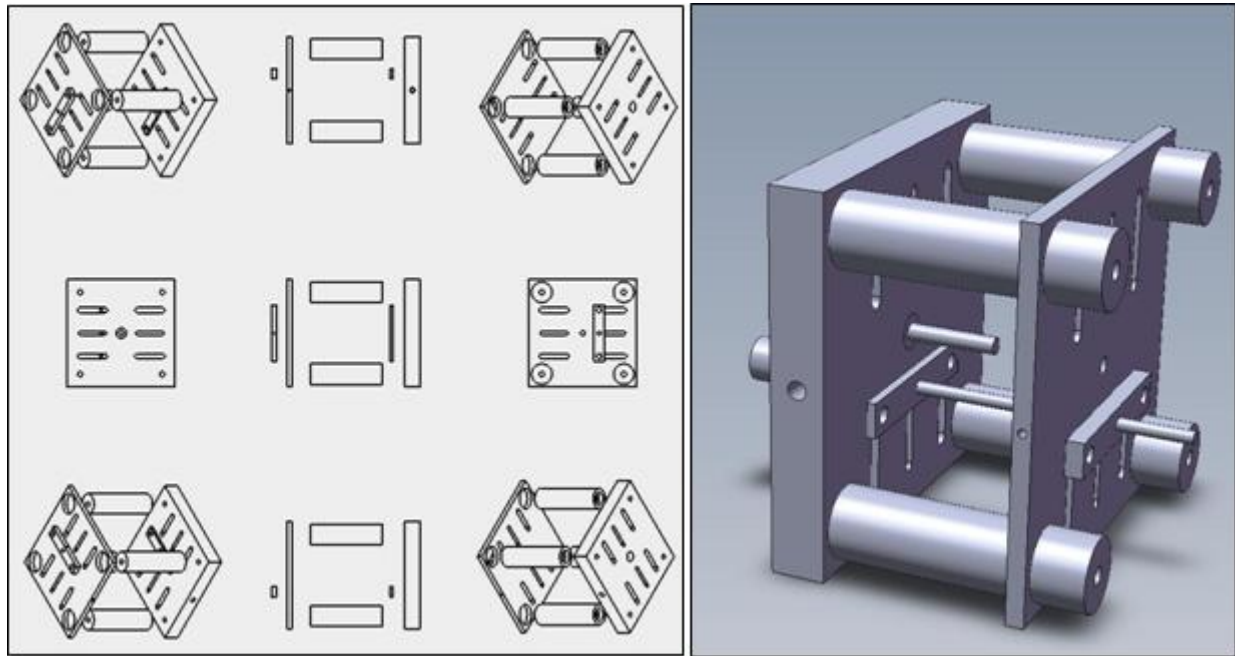


Figure 11: Transverse Mechanism Exploded and Isometric Views

Hot-Film Anemometer Data Acquisition System

The anemometer used in these experiments was TSI's IFA 300 constant temperature anemometer (CTA), with two active channels. The IFA 300 uses a Wheatstone bridge configuration to maintain the sensor at a constant resistance. The voltage required to maintain this resistance, referred to as the bridge voltage, is recorded and is the raw data of the system. The IFA 300 contains internal signal conditioners which allow the bridge voltage to be amplified and shifted to match the range of the data acquisition card for higher resolution output [10]. The data acquisition card used was the UEI 4 channel $\pm 5V$ PowerDAQ II supplied by TSI. The acquisition software employed was TSI's ThermalPro for Windows XP. This software was

responsible for setting the operating conditions of the probe, configuring the sampling conditions for data acquisition, triggering the anemometer, and recording the voltage data.

TSI's 1244-20W hot film probe was used for the purposes of this research, which consists of two platinum coated quartz tube (50.8 μ m dia) sensors in a parallel alignment. The sensors have a 1.02 mm sensing length, and are at a distance of 1.016 mm in the streamwise direction. Each sensor on the probe occupies its own channel on the IFA 300 cabinet and A/D converter board.

High Speed Camera

The high speed camera employed was a Fastec Troubleshooter (model: TSHRMM), which contains a CMOS array, and records up to a resolution of 1280 x 1024 pixels, with 8-bit pixel resolution in monochrome and 24-bit pixel resolution in color. The Troubleshooter is a standalone device containing its own data storage device (3GB), and a display for viewing and editing footage directly after recording. The camera was mounted on a tripod, facing the opposite side of the channel from which the transverse mechanism was mounted to obtain a clear view of the flow. A blank piece of white poster board was placed behind the channel to offer a solid background, at a distance far enough away such that shadows would not be cast on it. A function generator was used for external triggering, to avoid handling of the camera which could cause motion during recording or resetting of the camera position. Two 27W (120 V 60Hz) compact fluorescent lamps were used for lighting, positioned above and below the area of interest to shed a blanket of even lighting. Though the recording frequency was greater than the

frequency of the AC bulbs, the flickering was found to have minimal effect due to the quality of the backdrop and the strength of image processing system.

HFA Signal Analysis

Phase Discrimination and Void Fraction

For the purpose of signal slope based phase discrimination, a program was generated that would crawl through the first derivative of the signal, looking for spikes that reached the slope threshold in both the negative and positive directions, signifying the arrival or passage of a bubble respectively. When the spike was negative, this was considered to be the result of the signal transitioning from the liquid phase to the gaseous phase. In this case, the program would back up through the data looking for the derivative of the signal to switch to positive, signifying the instant the sensor came into contact with the front edge of the bubble, and then would crawl forward looking for a second point where the derivative of the signal again switched to positive, signifying the instant the sensor came into contact with the rear edge of the bubble. This portion between the two sign changes was denoted as 0's in the phase indicator, indicating the gaseous phase. A similar scenario occurred when the program came across a positive spike, instead working in the reverse, finding the rear edge of the bubble, and crawling back to the front edge. The exact transition of negative to positive slope was actually selected by the slope reaching a value of positive ten, to avoid false triggers due to small noisy voltage fluctuations occurring in the low slope portion of the bubble, as suggested by [18]. The hybrid method was triggered by the signal dipping below the amplitude threshold value, and again following a similar pattern as the slope method to adjust the edges of the bubble interaction. Upon the trigger, the program would first walk backwards through the signal until the slope of the signal reach the value of

positive ten, as was previously done to denote the beginning of the bubble. The program would then go back to the instance of crossing the amplitude threshold and then continue until it came back above this threshold, as the signal approached the normal liquid voltage level. This point does not actually correspond to the edge of the bubble, so it would again crawl backwards until the slope reached a value of negative ten, to indicate the point at which signal started increasing upon the sensor first touching liquid. The program would then go back the second triggering event to crawl forward looking for more triggers, as to not be triggered by the same point.

The selection of the trigger threshold was a unique method based on the method employed by [23] for selecting an amplitude threshold, in which the void fraction was calculated for a range of amplitude threshold values, and the threshold being selected by the shape of the resulting curve. In this case, it was applied to the slope threshold as well, calculating the void fraction for various values and the appropriate threshold was taken from the features in the curve. What is unique in this study was differentiating the void fraction vs slope threshold curve in order to reveal further features.

Void Fraction

To calculate the local void fraction, the number of points listed as 0 in the phase indicator were counted, and divided by the total number of points in the sample. For the non-local void fraction, data sets were taken for various points across the channel, and the local void fractions were then integrated across the area of the channel using a Trapezoidal Riemann Sum method.

Bubble Speed

A discrete, normalized cross-correlation function was used to find the most probable time-shift of the bubble passages between the two parallel sensors. Because the sensors run at different operating resistances, due to the inherent uniqueness of any hot-film sensor, the signals occur across different voltage ranges, and thus the exact signal amplitudes are not comparable. To help the correlation, the signals are first normalized by subtraction the mean, and dividing by the standard deviation. The correlation function then integrates the product of the normalized signal of the first sensor and the normalized time-shifted signal of the second sensor over the entire data set. This integration is done for a range of time-shifts, and the time-shift that yields the highest correlation is selected as the average time taken for a bubble interface to pass between both sensors. The bubble speed is then calculated from the time taken to pass between sensors, and the known distance between the sensors. It is also not trivial to again point out that this cross correlation was applied directly to the normalized voltage signals, and not to the phase indicator function. In some instances researchers employing the cross-correlation method choose to run the correlation for the phase indicator function, but in the present case it was found that the signal of the downstream sensor was not ideal for the generation of its own phase indication function. This is the method successfully employed by van der Welle [26], Wang-Ching [27], and [28]. The normalized cross correlation function used in this case can be seen in Equation 1.

$$R(\tau) = \frac{1}{T_{tot}} \cdot \int_0^{T_{tot}} \frac{(V_1(t) - \mu_1) \cdot (V_2(t + \tau) - \mu_2)}{\sigma_1 \sigma_2} \cdot dt$$
$$R(\tau) = \frac{1}{T_{tot}} \cdot \sum_{t=0}^{T_{tot}} \frac{(V_1(t) - \mu_1) \cdot (V_2(t + \tau) - \mu_2)}{\sigma_1 \sigma_2}$$

Equation 1: Normalized Cross Correlation Function for Most Probable Interfacial Time-shift

Bubble Size

The residence time of a bubble refers to the amount of time the sensor spent sensing the bubble. The chord length of a bubble detected in the signal is then calculated from its residence time and the known bubble speed. The program crawls through the phase discriminated data plucking out bubble interactions and recording its residence time, the bubble interactions are noted by being lengths of zeros (gas) booked ended by ones (liquid). The number of consecutive samples denoted as zeros divided by the sampling rate, gives the residence time of a single bubble. Once all of the residence times are collected, a straight average is taken, and multiplied by the bubble speed to give the average chord length. This chord length can be interpreted a few ways depending on the study, and in this case was considered to be the longest diameter of the bubble, pressed between the narrow walls.

High Speed Camera Image Analysis

High speed video was taken at 500fps with a 640x480 resolution (monochrome), to obtain a recording time of 26 seconds. Images of the flow were taken for the first 10 seconds of recording, and then the air was shut off, allowing the system to come to a single-phase liquid flow over the remaining video timing. This was done in order to obtain a clean image of the channel with no bubbles in it to serve as a frame of references for the rest of the images. The high speed images were analyzed using MATLAB's image processing toolbox, generating a script that would quickly process and analyze the images. First the background reference image was subtracted from the rest of the images to remove the background noise and leave only the bubbles remaining. Edge detection was performed via the Canny function, using an adjusted

threshold to further remove noise. The Canny function employs two thresholds, one major threshold to find any strong edges, and a second minor threshold to find any weak edges that are touching any strong edges to connect the outline of the object with no gaps [29]. Each bubble outline was then filled in to mark each bubble as a clear single object in the image. The script would label each object found in the image, and then would provide information about each object, such as the centroid location, area, and dimensions. The image could then be displayed with each object given a distinct color, to give a quick look at the labeling. This color labeling was important in the velocity analysis, which made it possible to quickly check that a bubble maintained the same label through two consecutive images, following a left-to-right labeling order.

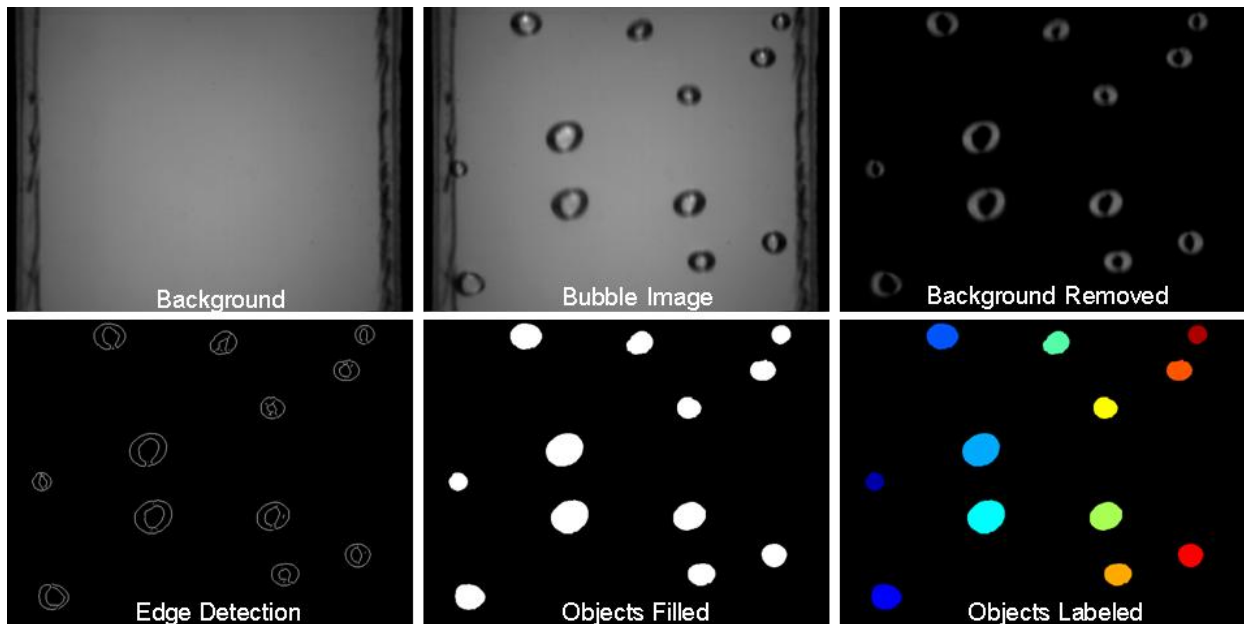


Figure 12: Image Processing Technique

The bubble diameter was taken as the diameter of the circle with an area equal to the area of the somewhat irregularly shaped bubble. The velocity was taken as the change in location of

the bubble's centroid in the streamwise direction over 10 frames. Void fraction was found from estimating the volume of the bubbles in the frame, and subtracting this from the known total volume of the frame. The estimation was done by calculating spherical volumes for any bubbles less than the depth of the channel (3.175 mm). For larger bubbles the exposed area was multiplied by the channel depth, assuming the volume difference due to the curved edges to be small compared to the rest of the bubble touching the walls of the channel.

While the image processing calculated the distances in number of pixels, the length of each referred pixel was found from measuring the channel width from the background image, relating the known width of the channel to the length in pixels shown in the images. The pixel length ratio was calculated from the background image for each set of recordings to account for any small changes in the camera position or focus between data sets.

CHAPTER FOUR: RESULTS AND DISCUSSION

Cases Run

Tests were performed for different superficial liquid and gas velocities to obtain varying flow volume fractions. The parameters were chosen based on the ranges that stayed within the boundary of bubbly flow regime, as provided by Mishima's flow regime maps for rectangular channels with 2.4 mm and 5.0 mm gaps [12]. The range of velocities and subsequent volume fractions examined can be seen below.

Table 1: Test Matrix

Test #	Q-l (L/min)	Q-g (L/min)	j-l (m/s)	j-g (m/s)	j (m/s)	Volume Fraction
61	1.336	0.030	0.184	0.004	0.188	0.022
62	0.980	0.031	0.135	0.004	0.139	0.030
60	1.333	0.081	0.184	0.011	0.195	0.057
68	1.030	0.084	0.142	0.012	0.154	0.076
49	1.179	0.100	0.162	0.014	0.176	0.078
50	0.981	0.084	0.135	0.012	0.147	0.079
30	0.980	0.084	0.135	0.012	0.147	0.079
39	1.031	0.103	0.142	0.014	0.156	0.091
28	0.978	0.102	0.135	0.014	0.149	0.094
45	0.981	0.102	0.135	0.014	0.149	0.094
48	1.233	0.129	0.170	0.018	0.188	0.095
37	1.082	0.129	0.149	0.018	0.167	0.107
32	1.080	0.129	0.149	0.018	0.167	0.107
44	1.031	0.129	0.142	0.018	0.160	0.111
38	1.029	0.130	0.142	0.018	0.160	0.112
46	1.277	0.163	0.176	0.022	0.198	0.113
34	0.977	0.128	0.135	0.018	0.152	0.116
36	0.984	0.129	0.136	0.018	0.153	0.116
35	0.976	0.129	0.134	0.018	0.152	0.117
33	0.984	0.132	0.136	0.018	0.154	0.118
29	0.980	0.134	0.135	0.019	0.154	0.121
52	1.127	0.162	0.155	0.022	0.178	0.126
47	1.329	0.193	0.183	0.027	0.210	0.127
42	1.080	0.161	0.149	0.022	0.171	0.130
40	1.031	0.162	0.142	0.022	0.164	0.136

51	1.185	0.193	0.163	0.027	0.190	0.140
53	1.130	0.194	0.156	0.027	0.182	0.147
43	1.080	0.193	0.149	0.027	0.175	0.152
31	1.080	0.193	0.149	0.027	0.175	0.152
63	1.077	0.193	0.148	0.027	0.175	0.152
67	1.032	0.190	0.142	0.026	0.168	0.155
54	0.980	0.197	0.135	0.027	0.162	0.167
58	1.328	0.296	0.183	0.041	0.224	0.182
56	0.975	0.255	0.134	0.035	0.169	0.207
66	1.033	0.307	0.142	0.042	0.185	0.229
59	1.139	0.372	0.157	0.051	0.208	0.246
64	1.036	0.431	0.143	0.059	0.202	0.294
57	0.957	0.439	0.132	0.060	0.192	0.314
65	0.957	0.521	0.132	0.072	0.204	0.353

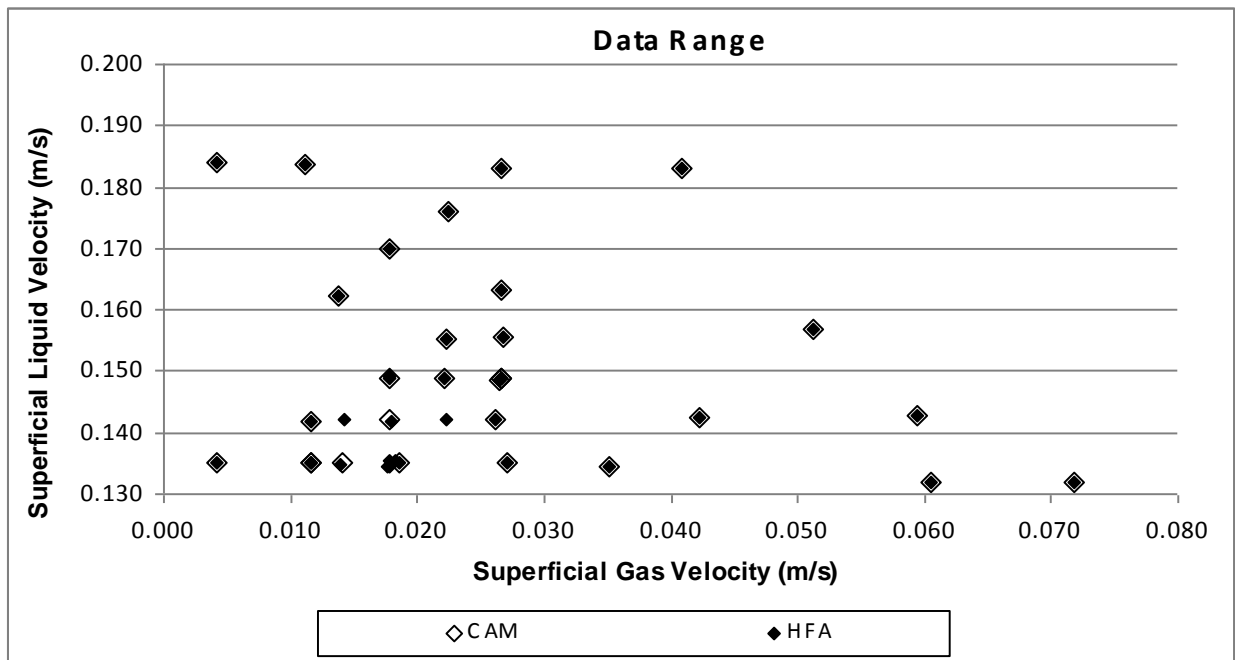


Figure 13: Map of Superficial Liquid and Gas Velocities Examined

Some sample images from the high-speed video results can be seen below, illustrating the wide-range in bubbly flow regimes studied.

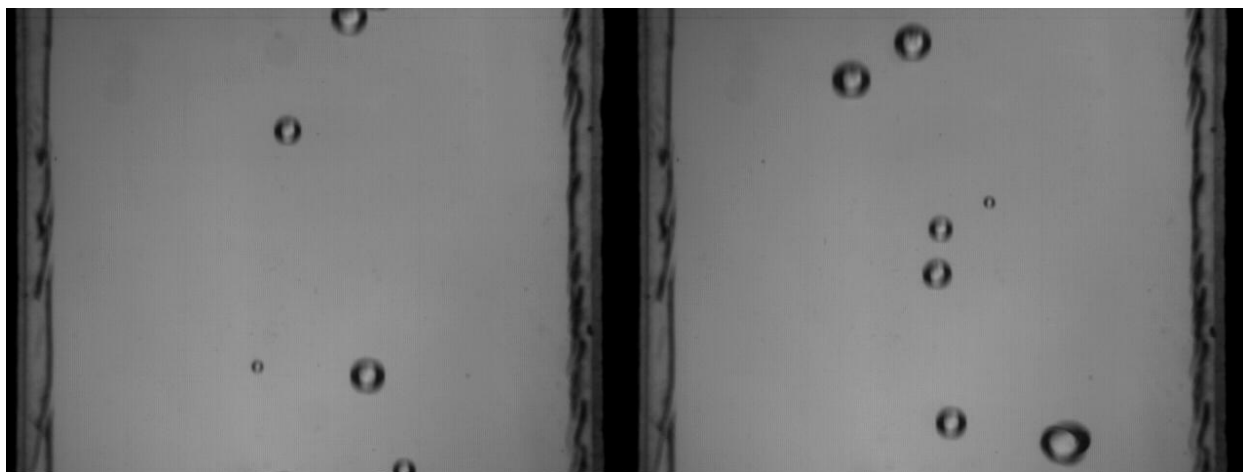


Figure 14: Sample Images from Volume Fraction of 2.2%

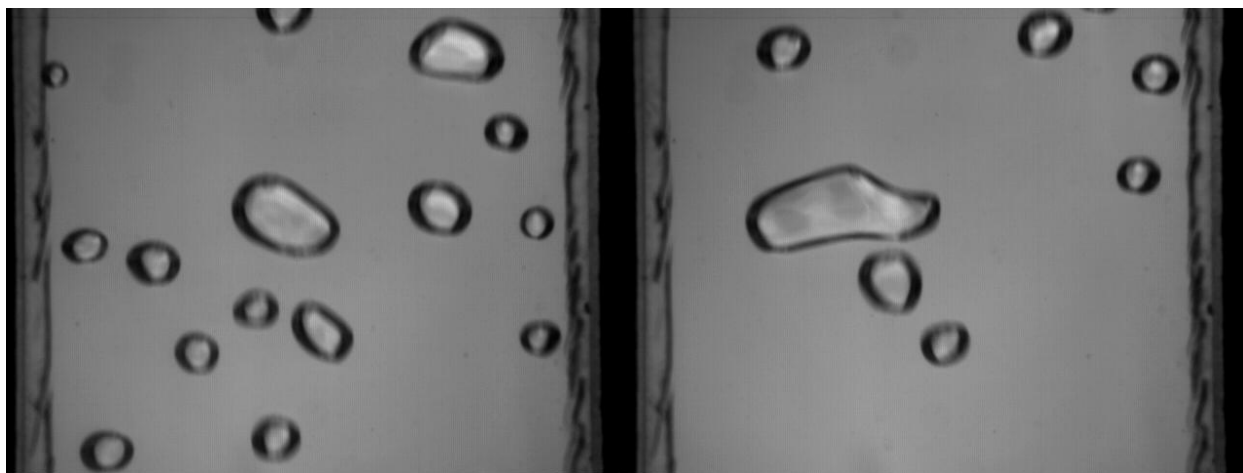


Figure 15: Sample Images from Volume Fraction of 15.2%

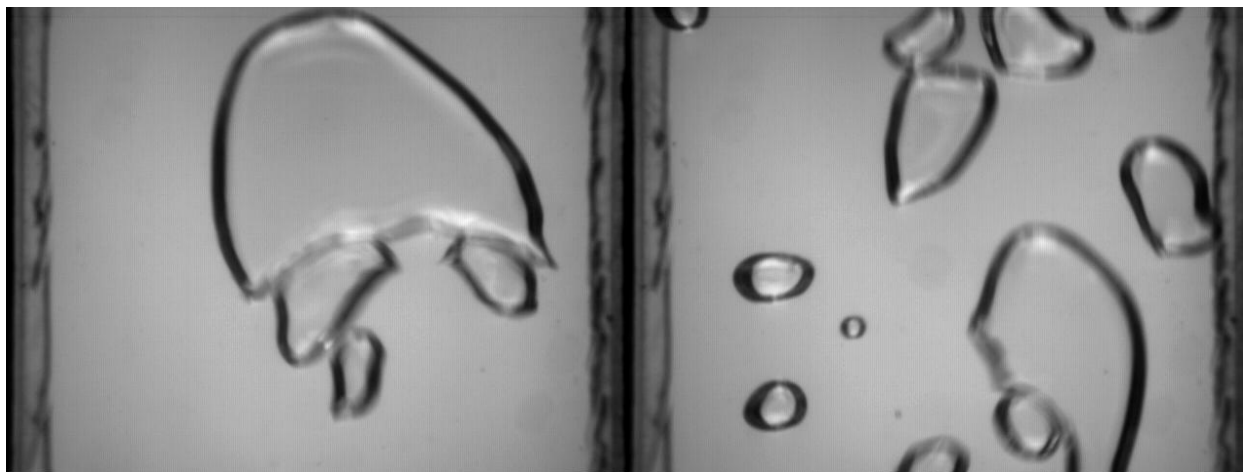


Figure 16: Sample Images from Volume Fraction of 35.3%

Comparison of Phase Discrimination Methods

The two general methods to distinguish between the phases within the signal involve either looking at the signal amplitude, or the signal slope (amplitude-time derivative). A typical sample of the signal amplitude can be seen below, showing two seconds of a flow with a volume fraction (β) of 14.7% (Test-53). Overlaid on the signal are the various threshold levels to be described in detail in the following discussion and analysis, for which figures generated from this typical signal are shown.

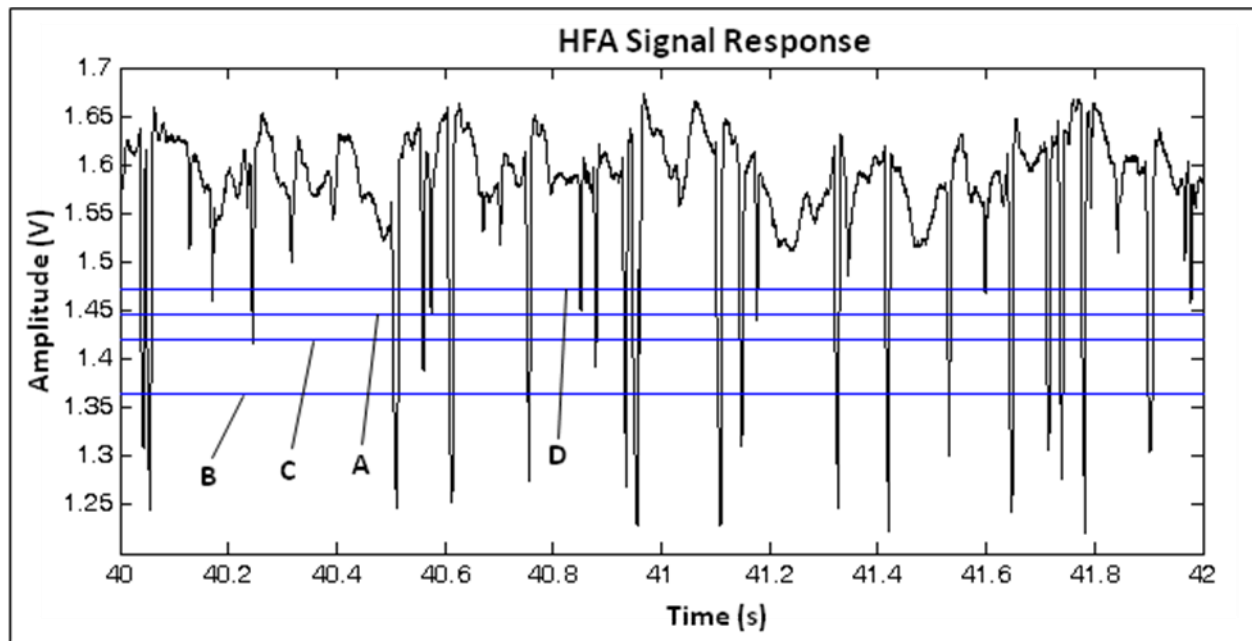


Figure 17: Sample of Hot Film Anemometer Signal Response - Amplitude

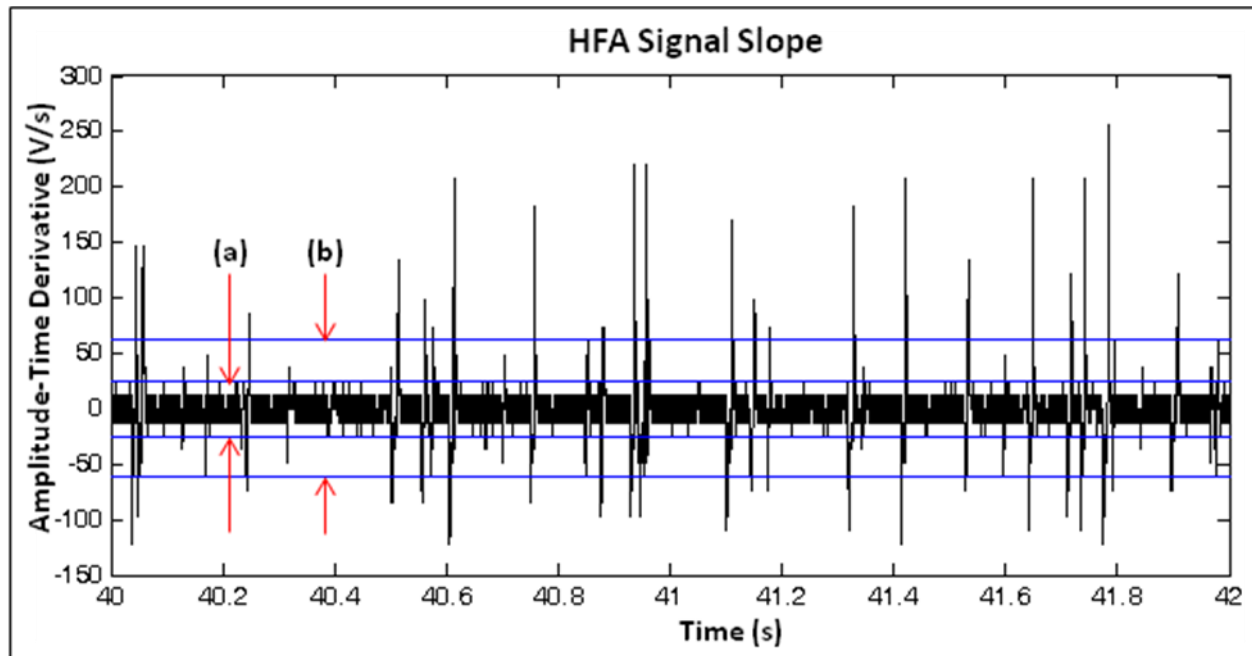


Figure 18: Sample of Hot Film Anemometer Signal Response – Slope

The first thing that is commonly looked at for an amplitude threshold value is the voltage histogram which shows two peaks, one corresponding to the most common gaseous phase voltage, and one for the most common liquid phase voltage. The area between is an overlap between the two phases, so a common and basic threshold value taken from this is the point halfway between the peaks, which will be considered here.

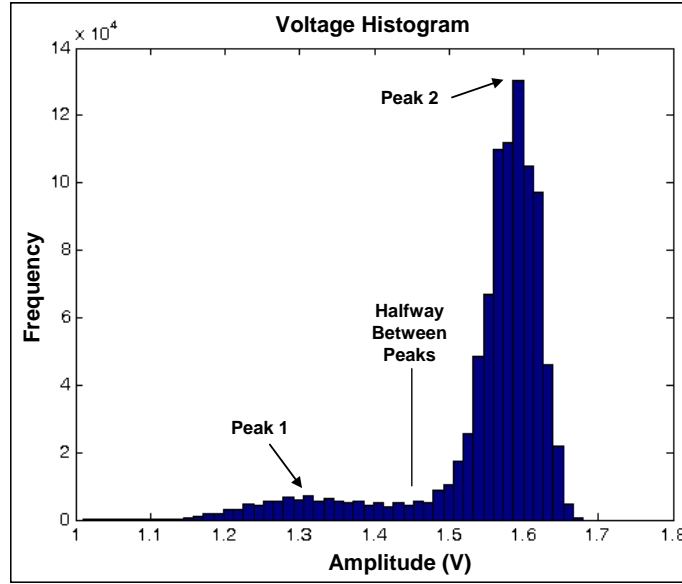


Figure 19: Amplitude Threshold Selection - Voltage Histogram

After running the code for the hybrid method of phase discrimination for a wide variety of threshold values, a few patterns and points of interest appeared. The typical resulting curves can be seen below detailing these points. Figure 20 shows that by increasing the threshold from the minimum voltage in the signal all the way to the maximum voltage the void fraction can range from zero to one. By looking at this derivative of this curve, shown in Figure 21, it is apparent that the derivative resembles the voltage histogram due to the nature of amplitude phase discrimination. The point shown as point A, is the point halfway between the peaks of the voltage histogram seen in Figure 19. Points B and D refer to the limits of the flat area between the two peaks, giving the most conservative and liberal estimations of threshold value that could be made. Point C is the lowest value of the derivative within the trough, which would be an inflection point and the point at which the void fraction changes the least due to changing threshold value. Though this point seems to be near the centered between B and D, it is often off to one side or the other depending on the nature of the peaks.

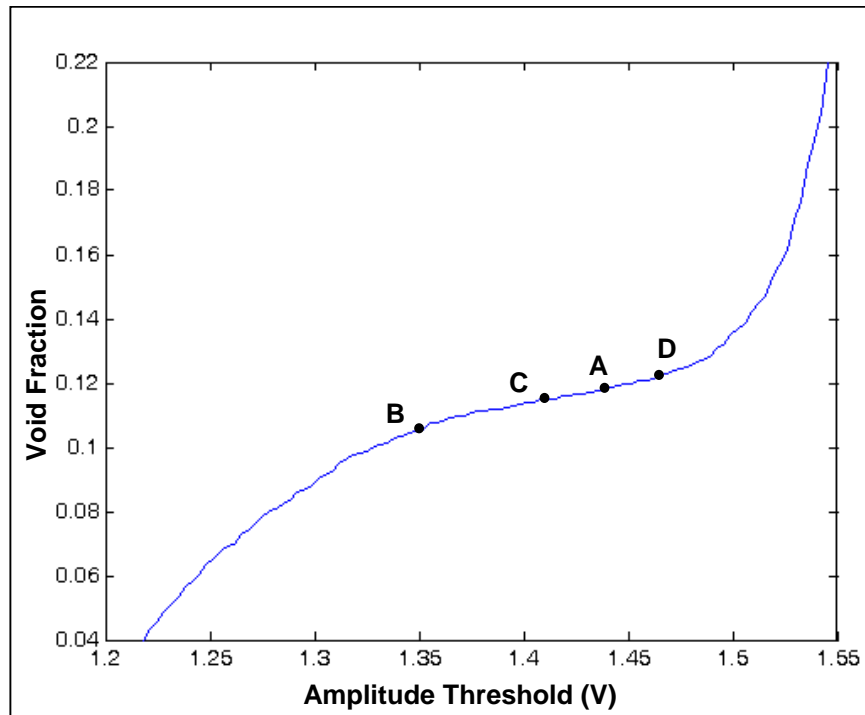


Figure 20: Amplitude Threshold Selection - Void Fraction vs. Threshold

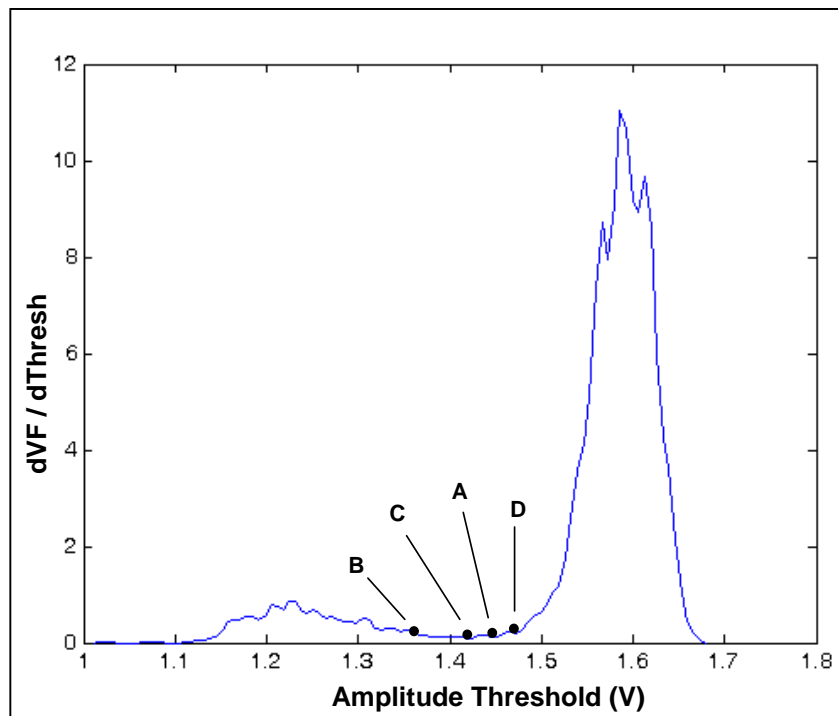


Figure 21: Amplitude Threshold Selection – Derivative of Void Fraction vs. Threshold

To be thorough, the effect on chord length of manipulating the threshold; a typical example can be seen below in Figure 22. It is clear that increasing the threshold has at least a slight effect of decreasing the chord length over the range of previously accepted threshold values. This can be explained by small bubbles and partial hits that would have smaller chords not causing a large enough drop in voltage to be picked up in high threshold values, or by turbulent effects in the liquid phase causing short durations of stagnant water that are not picked up by lower threshold values.

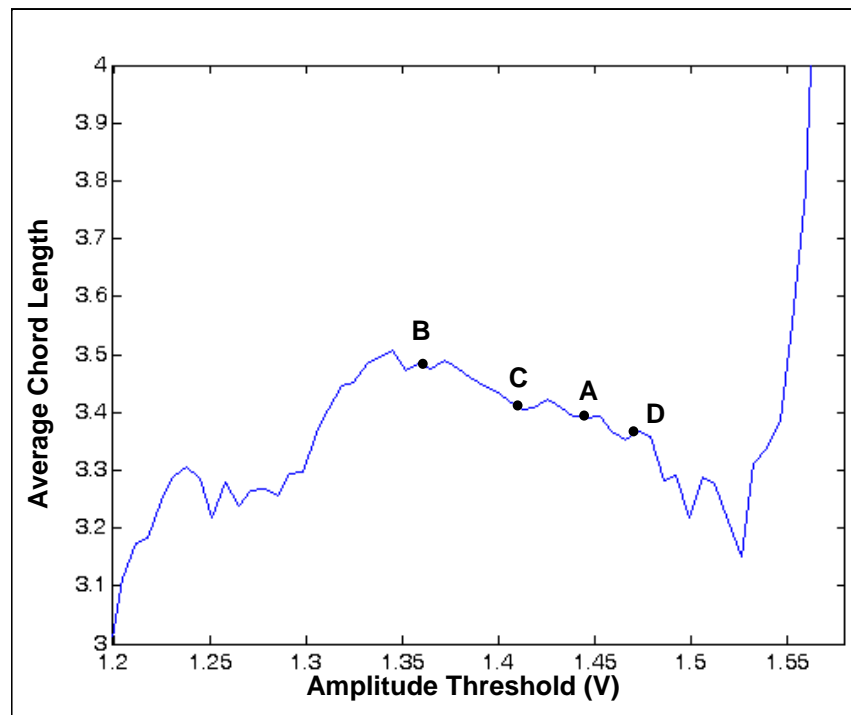


Figure 22: Amplitude Threshold Selection - Chord Length vs. Threshold

The same curves were generated for variation in the slope threshold value, and can be seen in the figures below. The first apparent feature is a very significant jump in void fraction after a very gradual increase with decreasing threshold, as can be seen in Figure 23. This phenomenon illustrates the threshold reaching low enough to include a natural fluctuation in the

system. The point just before this rise is of interest because it represents the most liberal slope threshold, denoted as Point (a). It is interesting to point out that unlike every other threshold, this one was found to be the same value (25 volt/s) for each case examined, spanning all flow conditions.

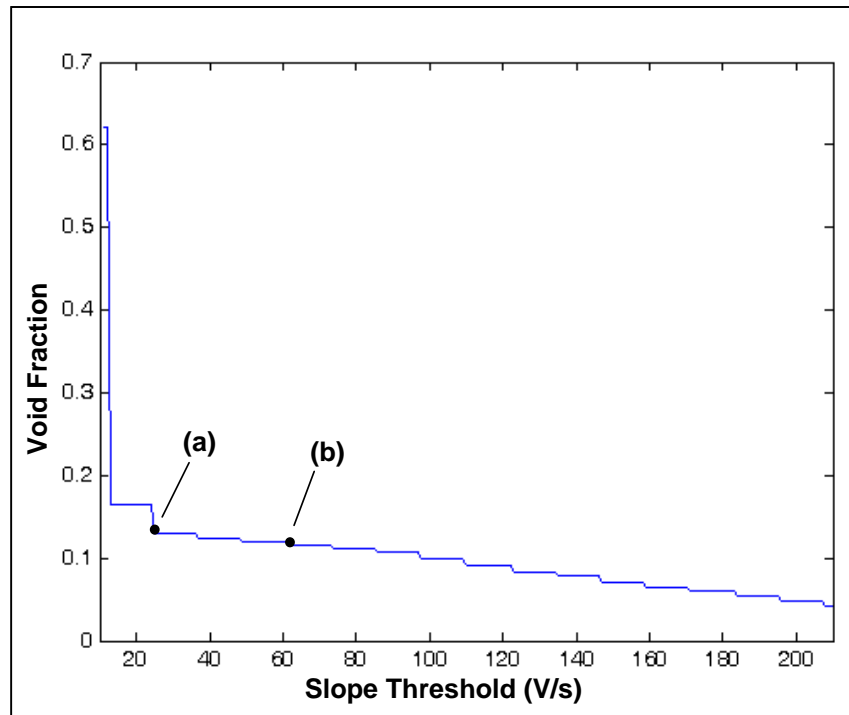


Figure 23: Slope Threshold Selection - Void Fraction vs. Threshold

The second point of interest is found on the plot of the derivative of the void fraction vs. threshold shown in Figure 24, there appears to be a trough akin to that seen in the derivative of the changing amplitude threshold value (Figure 21). The low point of this trough would indicate an inflection point, where the void fraction is least susceptible to changes in threshold value. This second point of interest for the slope threshold method, labeled point (b), is analogous to point C from the amplitude threshold method.

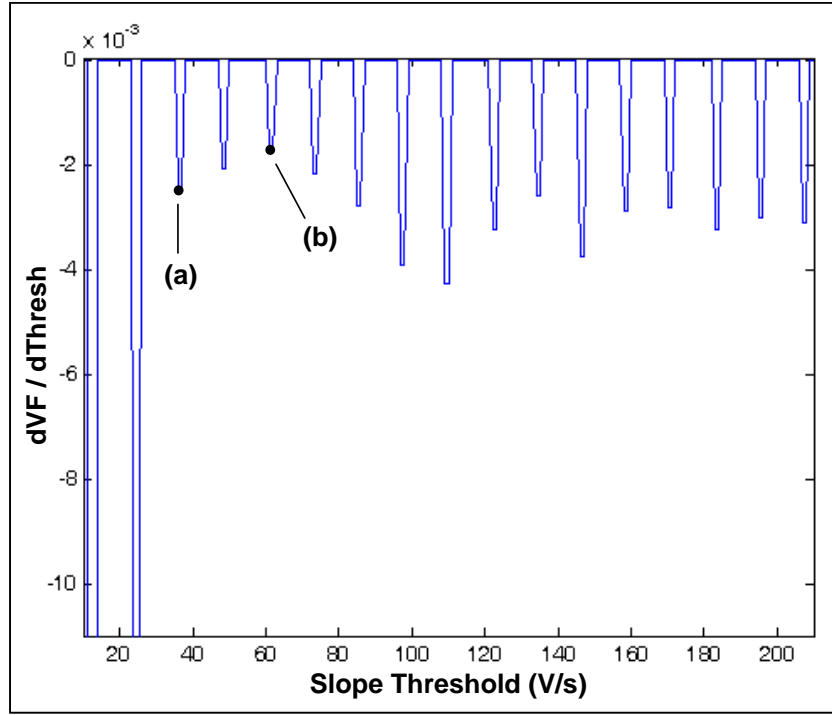


Figure 24: Slope Threshold Selection - Derivative of Void Fraction vs. Threshold

Again, as was done with the amplitude threshold case, the effect of changing the slope threshold on chord length can be seen in Figure 25. The sharp jump at point (a) is still apparent, resulting in a greatly decreased chord length explained by the lower slope threshold including the tiny ripples inherent to the system not associated with the gaseous phase.

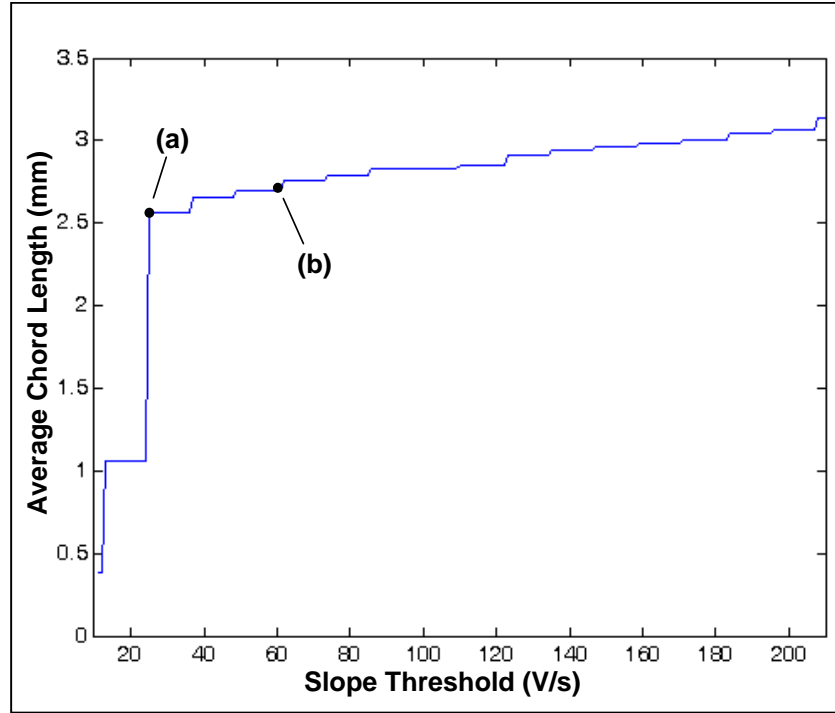


Figure 25: Slope Threshold Selection - Chord Length vs. Threshold

The comparison of the hybrid method with the amplitude threshold trigger and the slope thresholding method for the various threshold selection options can be seen tabulated in Table 2 with void fraction and chord length plotted in Figure 26 and Figure 27 respectively.

Table 2: Phase Discrimination Method and Threshold Selection Comparison

	Hybrid: Halfway Between Peaks (A)	Hybrid: End of First Peak (B)	Hybrid: Min. Between Peaks (C)	Hybrid: Beg. Of Second Peak (D)	Slope: Deriv. Min. (a)	Slope: End of Grad. Increase (b)	Relative Std. Dev. [All]	Relative Std. Dev. [Hybrid]
T-60: $\beta=.057$, $j-l=.184$, $j-g=.011$								
Threshold	1.4405	1.343	1.466	1.568	72	36		
Void Fraction	0.054	0.042	0.057	0.070	0.060	0.072	18.5%	20.4%
Chord Length	2.04	2.20	1.99	1.80	1.73	1.55	12.5%	8.1%
T-49: $\beta=.078$, $j-l=.162$, $j-g=.014$								
Threshold	1.4075	1.351	1.489	1.529	73	36		
Void Fraction	0.067	0.059	0.077	0.082	0.073	0.086	13.1%	14.1%
Chord Length	2.41	2.52	2.28	2.17	1.95	1.74	13.5%	6.6%
T-48: $\beta=.095$, $j-l=.170\text{m/s}$, $j-g=.018\text{m/s}$								

Threshold	1.4735	1.433	1.503	1.574	86	36		
Void Fraction	0.091	0.088	0.094	0.100	0.092	0.109	8.2%	5.8%
Chord Length	2.95	2.98	2.91	2.78	2.60	2.27	9.9%	2.9%
T-53: $\beta=.147$, $j-l=.156\text{m/s}$, $j-g=.027\text{m/s}$								
Threshold	1.4065	1.364	1.42	1.471	62	36		
Void Fraction	0.115	0.109	0.116	0.123	0.117	0.129	6.1%	5.3%
Chord Length	3.42	3.47	3.41	3.38	2.75	2.56	12.6%	1.2%
T-56: $\beta=.207$, $j-l=.134\text{m/s}$, $j-g=.035\text{m/s}$								
Threshold	1.4395	1.385	1.418	1.496	49	36		
Void Fraction	0.175	0.167	0.172	0.186	0.170	0.180	4.1%	4.7%
Chord Length	4.16	4.16	4.19	4.14	2.81	2.65	20.1%	0.4%
T-59: $\beta=.246$, $j-l=.157$, $j-g=.051$								
Threshold	1.4955	1.456	1.528	1.609	61	36		
Void Fraction	0.223	0.218	0.226	0.237	0.221	0.233	3.2%	3.6%
Chord Length	4.66	4.58	4.67	4.75	3.10	2.94	20.7%	1.5%

In the case of void fraction, all of the phase discrimination methods and threshold selection options are in close agreement, particularly at the moderate to higher volume fractions. A trend can be seen that as the volume fraction decreases, greater difference between methods is reported. This can be attributed to the weakening of the shape of the void fraction vs. threshold curve due to decreased bubble interactions giving a less pronounced gas phase portion. For the purposes of void fraction measurements, the choice of phase discrimination and selection of threshold value has little effect, though certain options provide for more liberal and conservative estimates.

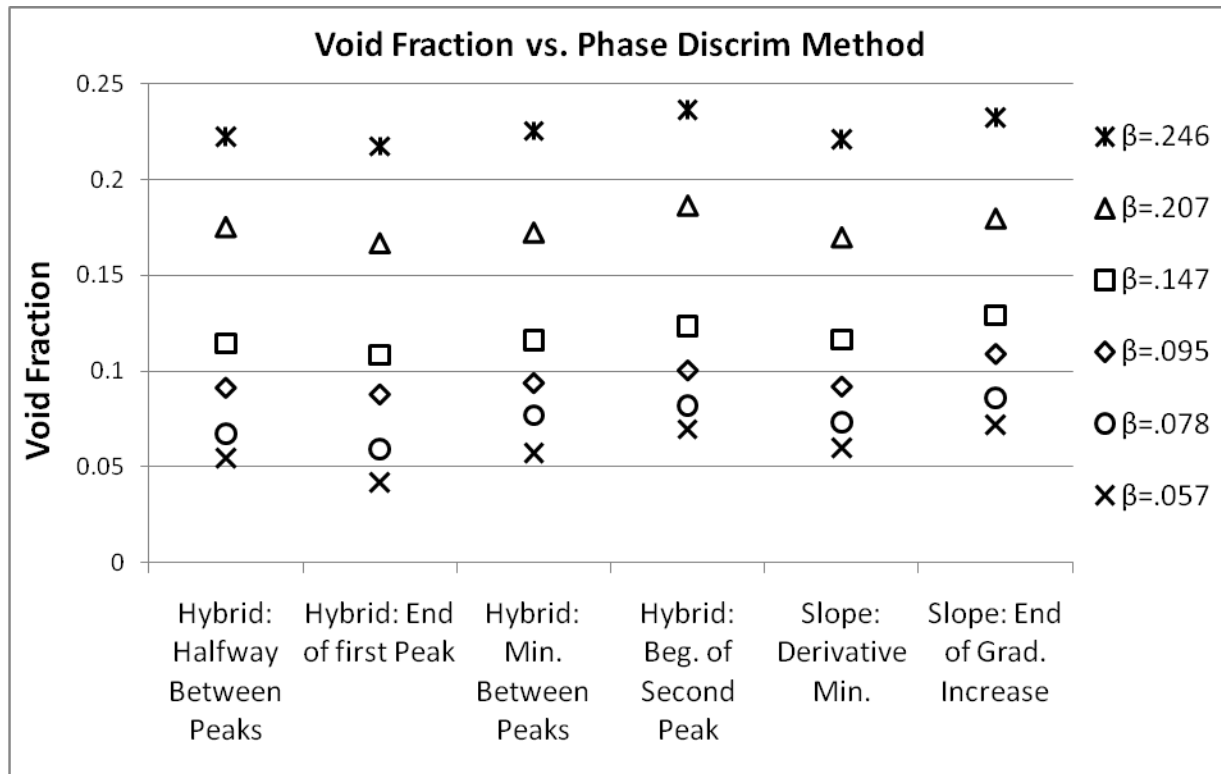


Figure 26: Threshold Selection Comparison - Void Fraction

The chord length results, however, show a large deviation for the slope based phase discrimination method. The tendency is for the chord lengths to be underestimated compared to the results for the hybrid method. Because the slope method indicates little to no change in chord length between volume fractions $\beta=.095$ and $\beta=.246$, it can be understood that the results using this technique are unfavorable for these testing purposes.

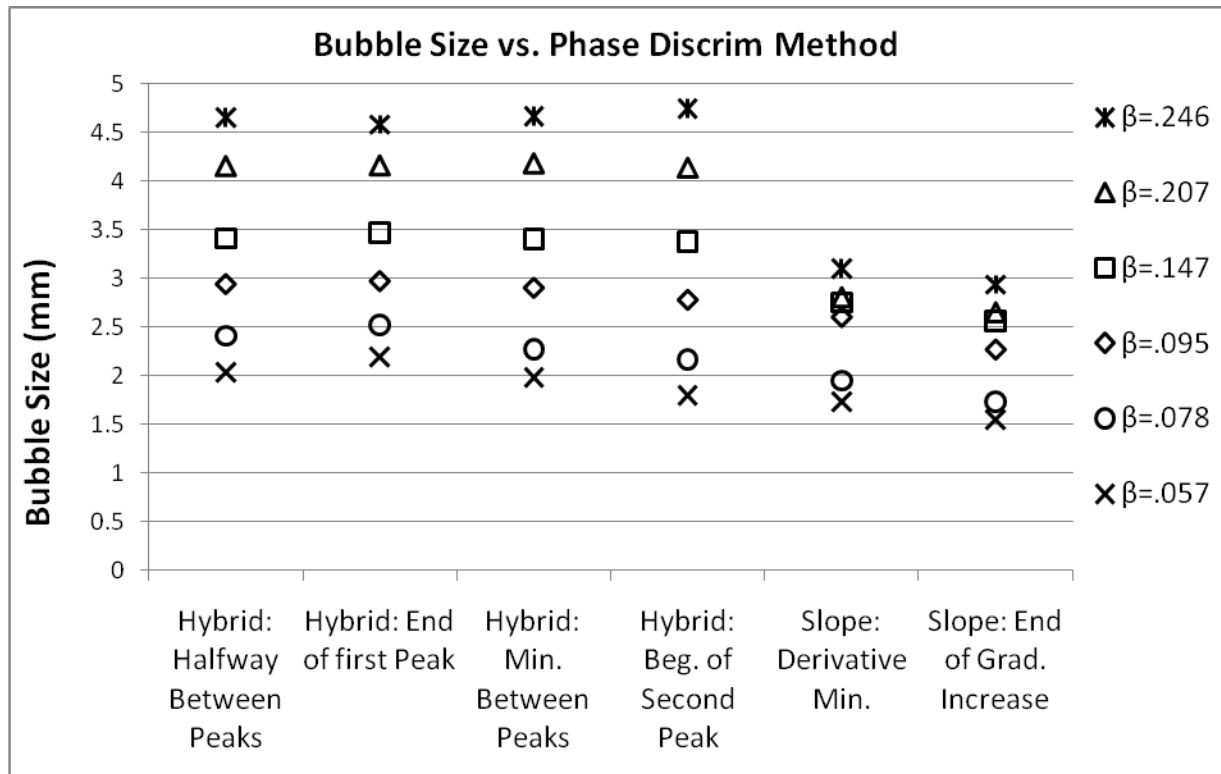


Figure 27: Phase Discrimination Method and Threshold Selection Comparison

The proper phase discrimination technique for the purpose of this study would then come down to a choice between the amplitude threshold selections using the hybrid technique. Being that they are in close agreement, for both void fraction and chord length, the choice is a matter of preference. The minimum in the trough of the void fraction vs. threshold derivative (point B) lends itself as being distinctly identified and having roots in physical principles as an inflection point where the bias of the liquid phase just begins to show an effect. The rest of the HFA results reported in this study come from the hybrid phase discrimination technique with the amplitude threshold being selected as the low point of the trough resulting from the differentiating the plot of void fraction vs. threshold.

Void Fraction

To compare the results of these tests, the drift flux model was used based on Ishii's parameters as applied to rectangular channels [14]. This model with the distribution parameter provided by Ishii can be seen in Equation 2. The 'j' refers to the superficial velocities, 's' is the narrow gap size (3.125mm), 'w' is the channel width (38.2mm), 'g' is the acceleration due to gravity, and 'ρ' is the density of each phase.

$$\alpha = \frac{j_g}{C_0 \cdot (j_g + j_l) + (.23 + .13s/w) \cdot \sqrt{\Delta\rho g w / \rho_l}} \quad C_0 = 1.35 - .35 \cdot \sqrt{\rho_g / \rho_l}$$

Equation 2: Drift Flux Model and Distribution Parameter for Rectangular Channels [14]

While some models predict void fraction (α) from volume fraction (β) by assuming a constant slippage ratio, the drift flux model accounts for variation in superficial velocities. So two cases with the same volume fraction can have somewhat different predicted void fractions based on the total mixture volumetric flux (superficial liquid velocity + superficial gas velocity). Volume fractions with a larger mixture volumetric flux will have a larger void fraction, due to less slip occurring between the phases. This is apparent in Figure 28 as the predicted values of void fraction by the correlation do not follow a strict linear relationship with the volume fraction, due to variations in the mixture volumetric flux.

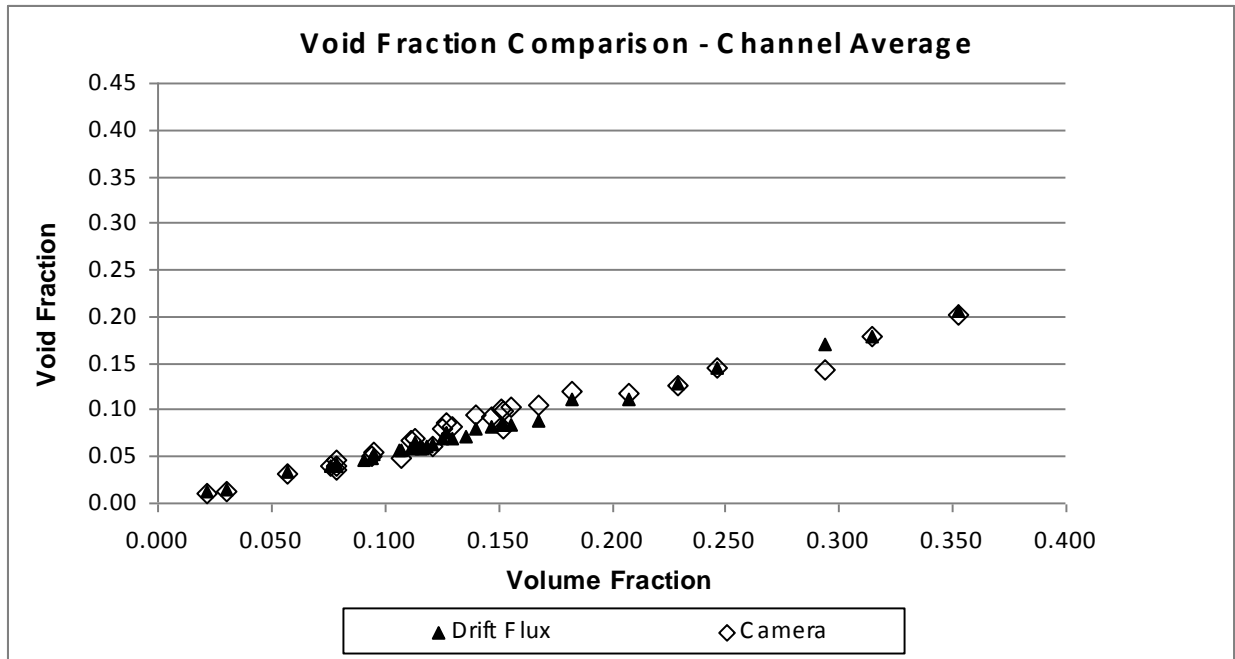


Figure 28: Channel Averaged Void Fraction Comparison

Figure 28 shows the results for the void fraction averaged across the channel-width as found from the high-speed camera tests. Close agreement is seen for the lowest void fractions, where the bubble sizes are small, however at higher void fractions, the camera begins to overestimate. This can be explained by the practice of considering bubbles with a diameter larger than the channel depth to be cylindrical, which estimates the bubbles to have a larger volume presence than if the curved edges could be accounted for. The differentiation between the two does remain below 30% in all cases.

The channel center, that is the center of the channel in terms of both width and depth, compares a location that both the HFA and high-speed camera take overlapping measurements. The projection of the bubble, as given by the high-speed camera gives the largest diameter of the bubble, which should be directly centered within the depth of the channel due to symmetry. The HFA can then be accurately placed in this depth center employing the calibration using the liquid

velocity profile as shown in Appendix A. Using this location the void fraction, bubble velocity, and bubble diameter can be directly compared between the two methods.

Sample cross-width profiles from the high-speed camera and cross-depth profiles from the HFA can be seen below for void fraction in Figure 29 and Figure 30 respectively.

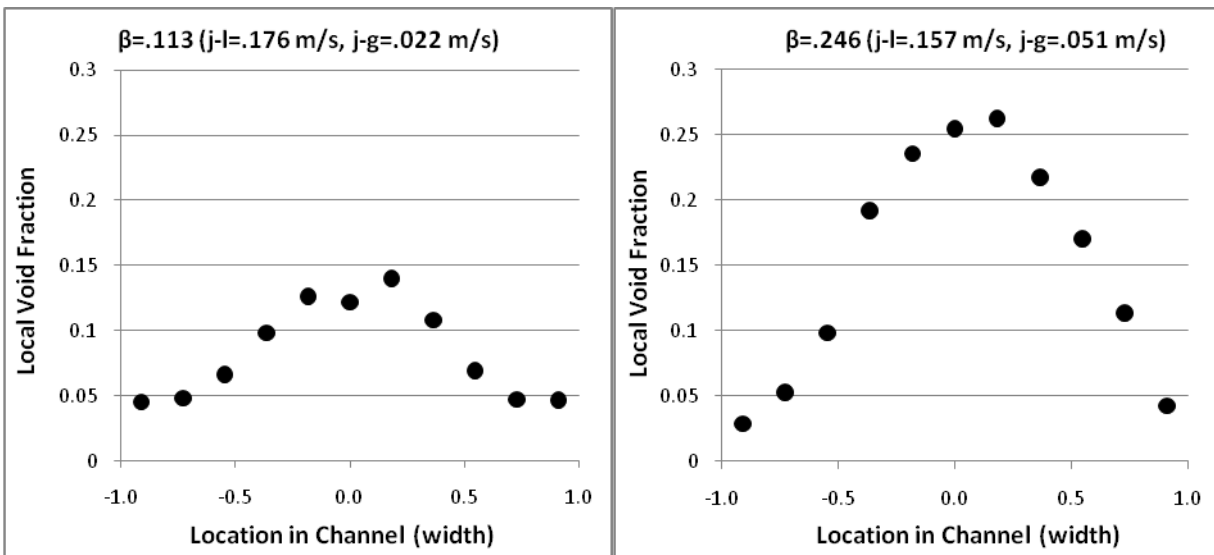


Figure 29: Sample Channel Width Void Fraction Profiles – High Speed Photography

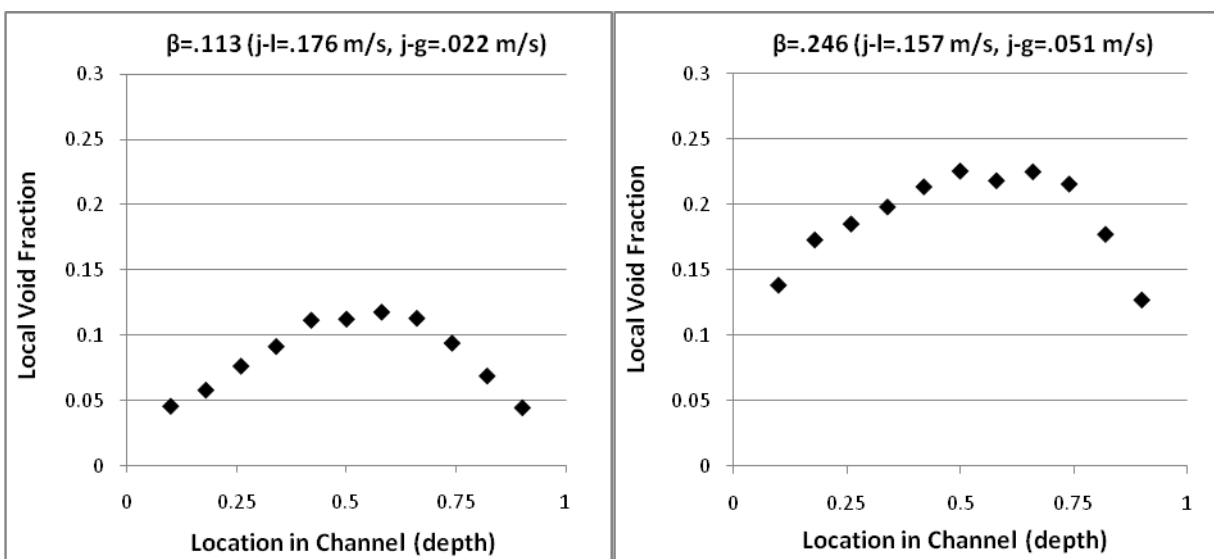


Figure 30: Sample Channel Depth Void Fraction Profiles – HFA

A slight bias towards the wall opposite to which the probe enters can be seen in the HFA profiles, which was typical of all cases examined. This can be described by the intrusiveness of the probe slightly deforming bubbles; as the gap between the probe supports and the wall decreases, the bubbles may have a tendency to narrow and length, exposing the sensor to air for an increased period of time. The effect is not dominating though, as the profile does still drop when reaching the far wall. The comparison between the two methods however, is at the mid-points of each profile. Shown in Figure 31 is the entirety of the results for the local center averaged void fraction as varied with volume fraction.

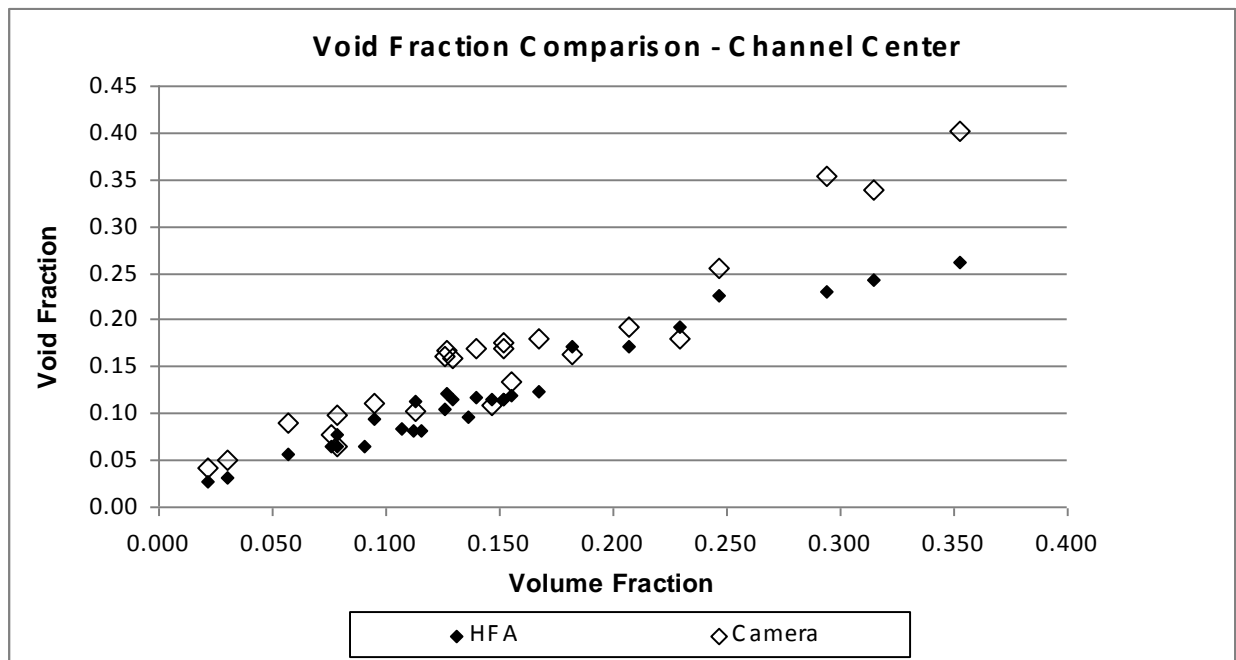


Figure 31: Channel Center Void Fraction Comparison

Bubble Speed

As discussed previously, the results for bubble velocity come from the comparison of the center portion of the camera results, relating to the hot-film sensor which is itself located in the channel centered width-wise. The channel was broken up into seven equally sized areas, with the center area being used for the comparison seen in the following results. Sample cross-width bubble velocity profiles can be seen below from the high speed photography, with bars displaying the standard deviation of the range of bubble speeds recorded in the sample at each location.

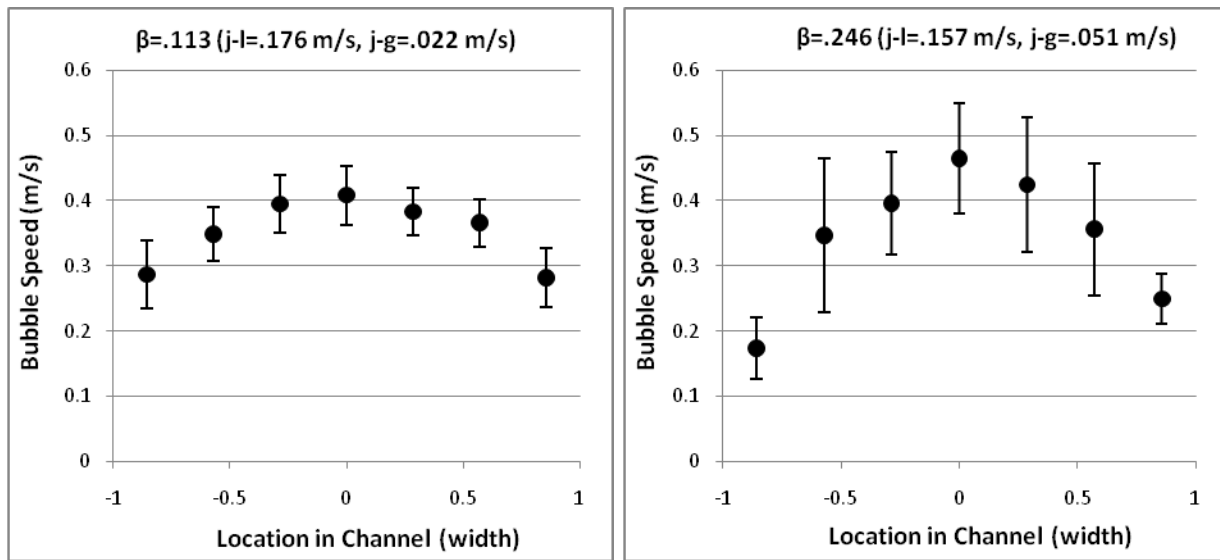


Figure 32: Sample Channel Width Bubble Speed Profiles – High Speed Photography (Bars show one std. dev.)

As can be seen the highest bubble velocity occurs at the mid-point, and is markedly decreased at the edges. This is expected due to the edge effects of the channel slowing down the flow and accelerating the core. The cross-depth profile resulting from the HFA can be seen below in Figure 33, which indicates a flat velocity profile across the depth of the channel. Again, this follows what is expected as the bubbles are large enough to span the narrow gap and

the velocity profile can be considered to be that of a single bubble's profile, which moves at one single velocity.

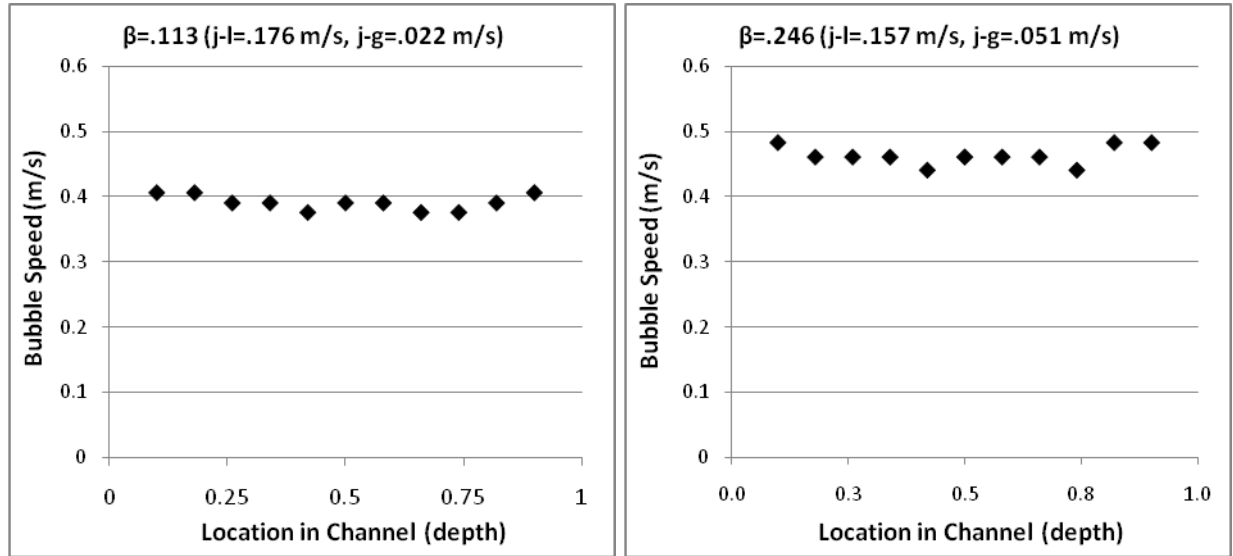


Figure 33: Sample Channel Depth Bubble Speed Profiles - HFA

Again, the best comparison of these two methods is at the mid-points of the profiles. The exhaustive velocity comparison can be seen in Figure 34 as it varies by volume fraction. Because the velocity is a function of not only by the volume fraction, but also the superficial liquid and gas velocities, the near-linear relationship shown for void fraction is not seen. The velocities reported by the two methods are in close agreement, and as seen in Figure 35, the difference between the two is less than 10% for volume fractions above .100, and below 30% in all cases examined. The reason for the increased error for lower void fractions can be attributed to the fewer interactions with the gas phase, making fluctuations from the liquid phase more prominent and less likely to be averaged out over even large sample sizes.

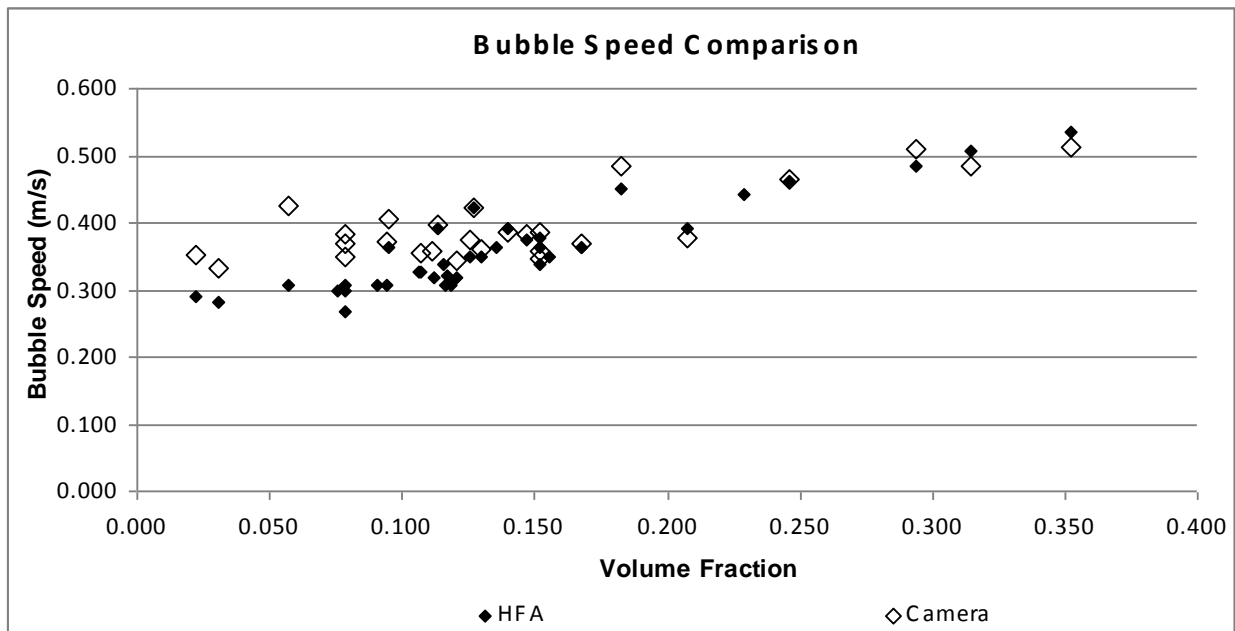


Figure 34: Bubble Speed Comparison - Volume Fraction

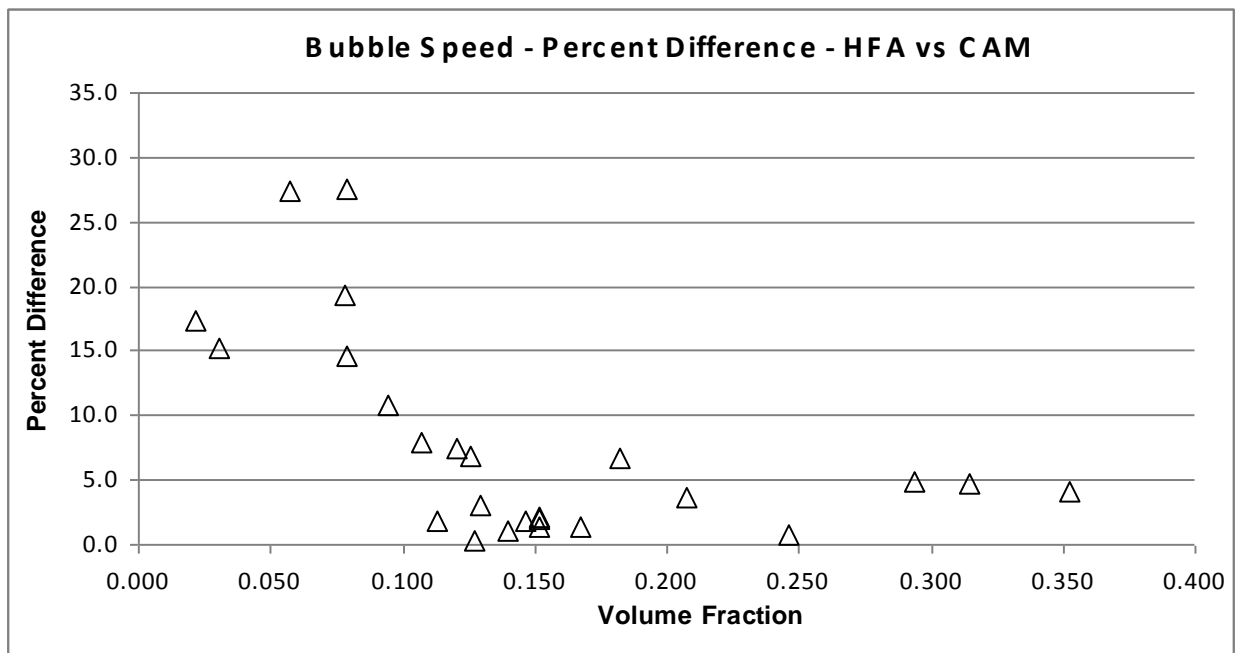


Figure 35: Bubble Speed Comparison – Percent Difference between HFA and High Speed Photography

Bubble Size

The bubble sizes profiles for cross-width and cross-depth can be seen below as provided by the high-speed photography and HFA respectively. The error bars show the standard deviation of the sample set for each location measured. Again, the important point of comparison is the mid-point of the profiles, due to the photographs showing the largest bubble diameter which should occur at the center location of the HFA profile.

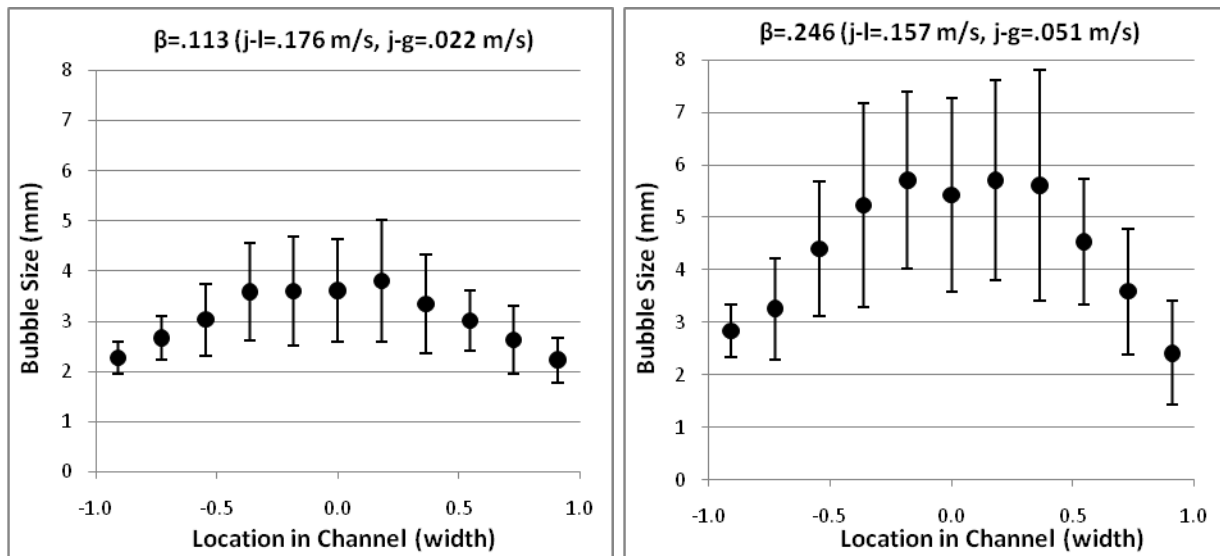


Figure 36: Sample Channel Width Bubble Size Profiles – High Speed Photography (Bars show one std. dev.)

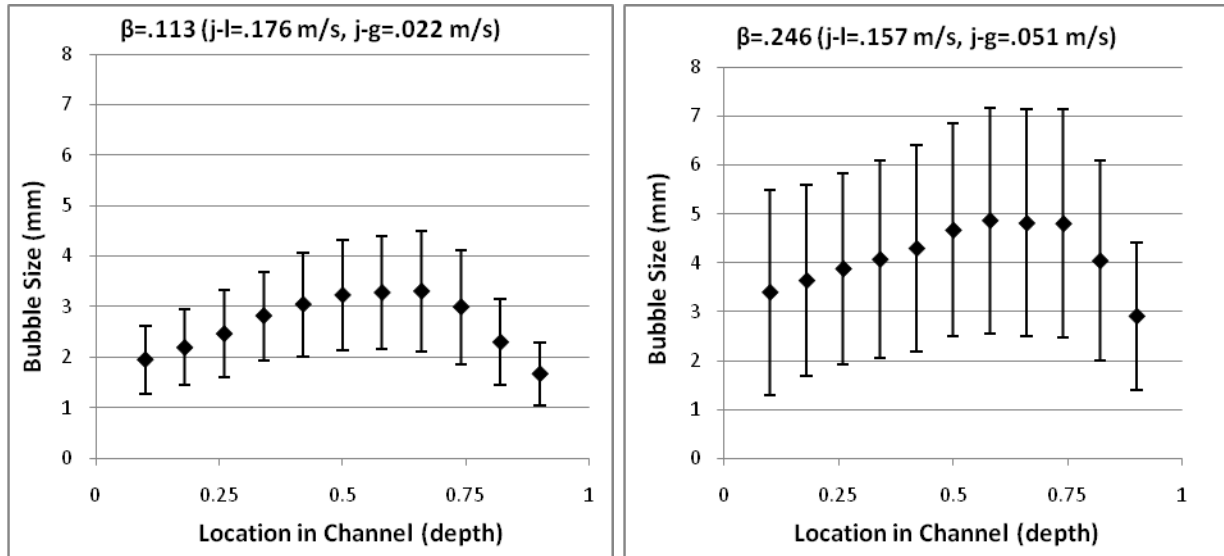


Figure 37: Sample Channel Depth Bubble Size Profiles – HFA (Bars show one std. dev.)

The slight bias to the far wall for the HFA results that was shown for void fraction once again is shown for the bubble size profile, due to the same deformation effect, with the bubbles having possibly having artificially higher chord lengths when pinched between the probe and the wall. The HFA profile does roughly resemble the leading edge of a bubble, as would be expected if the bubbles are bridging the gap within the narrow channel. Further, the high-speed camera profiles show maximum at the center of the channel as expected due to the higher rate of bubble-bubble interaction, encouraging coalescence. The comparison of center average bubble diameter can be seen below in Figure 38. The results from the high-speed camera are slightly larger in all cases, but increase with the same rate with volume fraction. The percentage difference between the two, as seen in Figure 39, has no trend with volume fraction and is evenly spread out across the data set. The bubble sizes from the imaging seem to be shifted upwards by a constant factor by around 1.3. Often in the use of hot-film anemometry for larger channels, the calculated bubble diameter is multiplied by a factor of 1.5 due to the probability of the sensor

piercing in between the longest diameter of the bubble (center) or somewhere along the edge. This statistical analysis is explained in detail by [30] and [31], but refers to a bubble variation in meeting the sensor in the depth direction where the sensor is the thinnest in direction. Due to the narrowness of the channel used in this study, this statistical method would not apply because the bubbles are very nearly the size of the channel or larger, so the probability of striking the longest diameter of the bubble in the depth direction is extremely high. However, there exists a probability that a partial hit could occur in the width direction where the sensor is longest and masked by the needles of the probe. The statistical analysis in this case is unclear because the geometry of the probe, and the ambiguity of the bubble interaction in the case of a partial hit in the width direction. Though this could explain an underestimation of the bubble diameter by a fixed factor on the part of the hot-film analysis.

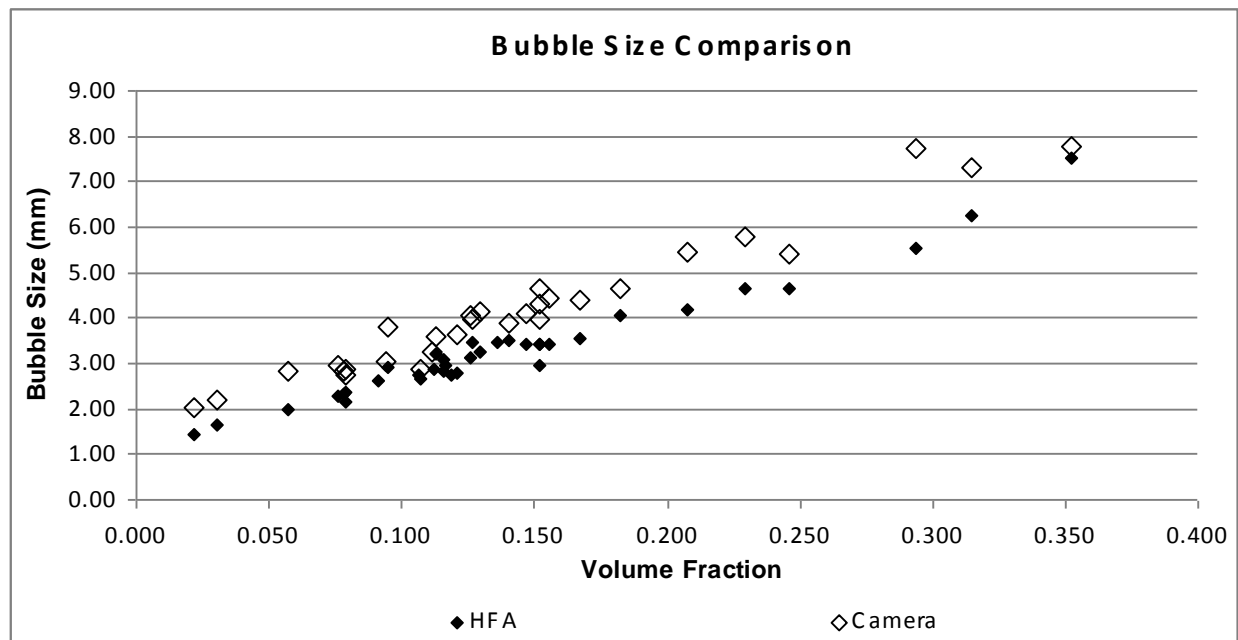


Figure 38: Bubble Size Comparison - Volume Fraction

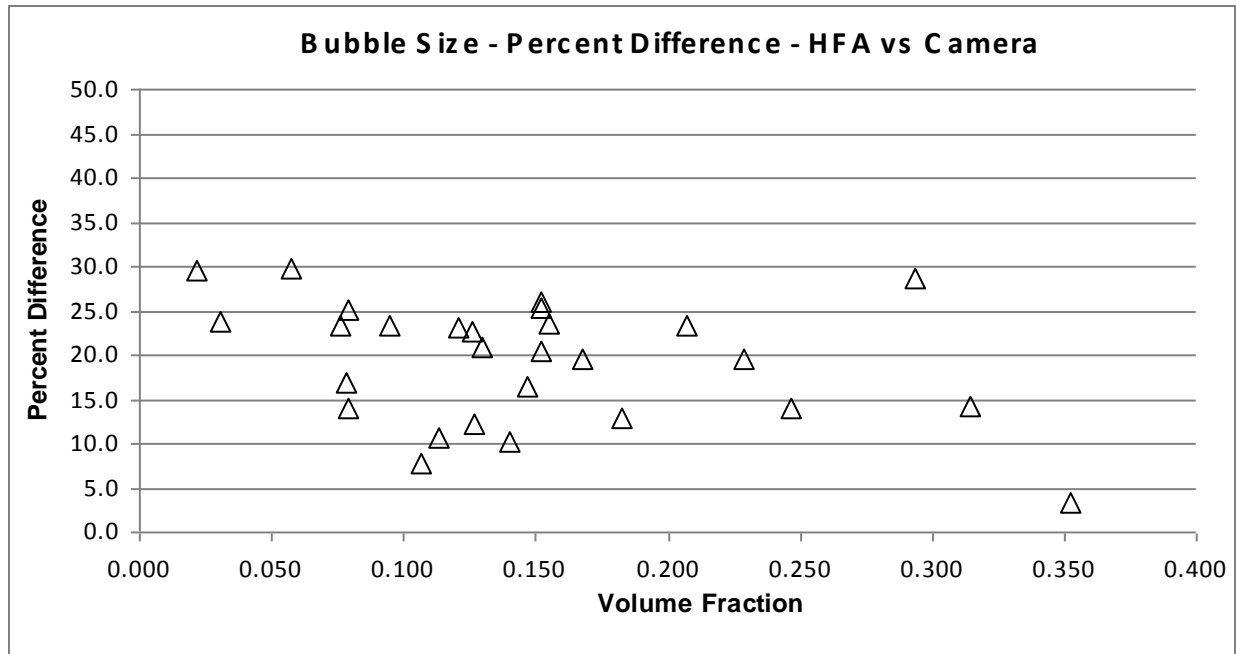


Figure 39: Bubble Size Comparison – Percent Difference

Though the results for the velocity show good agreement between the two methods, the results for the void fraction and bubble size demonstrate the differences that can occur. The strength of the hot-film is in the quick analysis of large amounts of data, recording nearly 1000 bubble interactions per sampling, though there is an ambiguous nature to each interaction for which assumptions such as threshold levels must be made. The high-speed video allows the direct examination of each bubble passage, though the processing is more tedious and is restricted to the analysis of only a few hundred bubbles. A longer sample time is favorable for void fraction measurements, which can be limiting for the high-speed photography that requires large file sizes and slow analysis.

CHAPTER FIVE: CONCLUSIONS

The hot-film anemometer is a well established method for use in multi-phase applications, and highly desired for its simplicity of operation and ability to quickly analyze large amounts of data. Multiple techniques have been established for the analysis of hot-film data by various studies, with the most important aspect involving separating the portions of the signal belonging to each phase. This study employed various techniques in order to demonstrate the use of the instrument, explore more deeply the methods of phase discrimination, and ultimately come up with a robust method of analysis favorable for the present geometry.

A vertically oriented acrylic test section with a narrow rectangular channel was connected to tightly controlled air-water flow loop for the purposes of studying and advancing hot-film anemometry techniques for multiphase flow. The narrow rectangular channel has applications for multi-phase heat transfer including miniature high-performance heat exchangers as well as for steam generation in the power generation industry. The geometry of the channel itself is also useful for the pairing of multiple measurement instruments, particularly optical devices, for the purposes of fundamental studies and demonstrations. This fostered ideal conditions for pairing high-speed video tests with the hot-film data for a large variety of flow conditions.

Through the study and comparison of phase discrimination methods and threshold selection, it was found that a hybrid technique was ideal for the current situation due to the hardships of a pure-slope technique in determining bubble diameters. The hybrid technique uses an amplitude threshold for triggering, and small slope thresholds for finely tuning the edges of the bubble interactions. This is a method first described by [18], and has since become widely

used. The method of amplitude threshold selection came from plotting the void fraction of the signal for a wide range of threshold values, as suggested by [23], but was taken a step further by differentiating this curve. It was found that the shape of the derivative consisted of two-peaks similar to that of the voltage histogram, with an inflection point in the trough between the two peaks. Though this study showed there were minimal effects in modifying the amplitude threshold within a range between these peaks, this inflection point was chosen for its easy of identification and consistency.

With a phase discrimination chosen and a robust method of threshold selection, a wide range of flow conditions were studied. Volume fractions ranging from 2% to 35% were studied, spanning across a range of bubbly flows. The void fraction comparisons were difficult due to the limiting nature of the high-speed video for processing large amounts of data, but the hot-film followed an expected trend and demonstrated high repeatability. The velocity was found to be in very close agreement between the HFA and high-speed video, staying within 10% for volume fractions above 10%, but still remaining under a 30% difference for even as low as the 2% volume fraction. The trends with volume fraction between the HFA and high-speed results were very similar, with the high-speed data seeming to be shifted off by a constant factor, but still remaining within the 30% range.

APPENDIX A: LOCATING CHANNEL CENTER

To be able to accurately relate the micrometer reading to the location of the probe sensor within the channel, tests were run to locate the exact center using the known principles of velocity profiles for fluids. The velocity profile is maximum at the center of the channel, so employing a pure water flow, the micrometer reading that reports the highest voltage would be the one that corresponds to the center. The location of the probe within the channel could then be known from the distance of the micrometer setting from the established reference point.

The first tests taken were a broad sweep across the channel, in order to find the general location of the peak. The second tests focused more closely on the area of the peak in order to pinpoint the exact location with a higher resolution. Because of the sensitivity of the probe and expected flat profile at the center of the channel, the tests were taken quickly to avoid the effects of any slight drift in temperature or flow rate, both of which were monitored closely. Samples were taken at 5000Hz for 13 seconds at each location, and the voltage value was taken as the average for each block of data. Both the temperature and flow rate were found to not fluctuate by more than 1% during the tests.

The tests were in good agreement with each other, pinpointing the center of the channel to correspond to the micrometer reading of .14 inches. Sample results can be seen below, one from the broad sweep, and one for the more focused sweep.

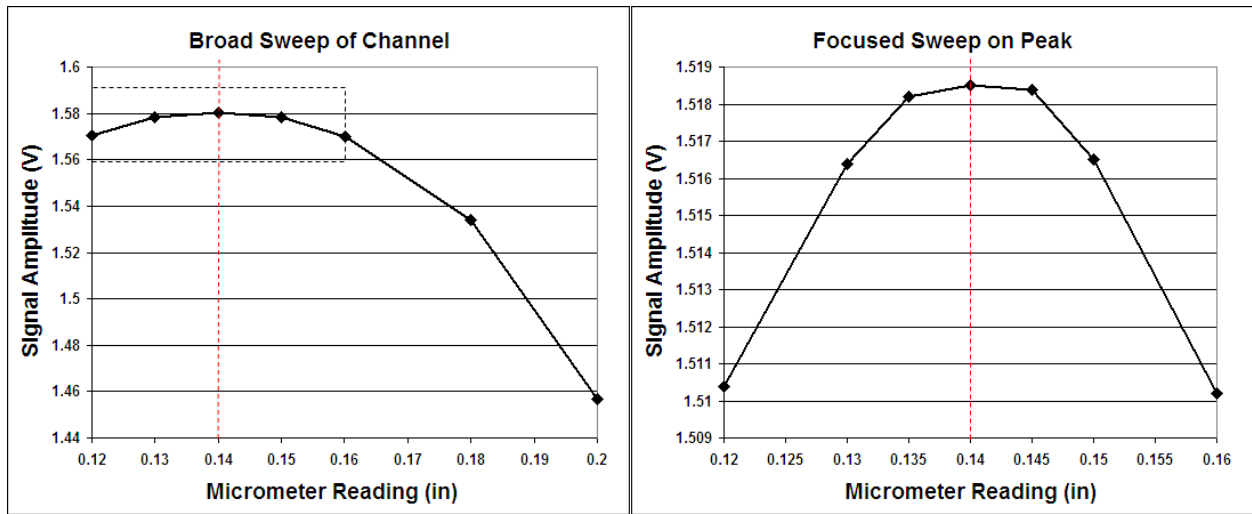


Figure 40: Channel Depth Tests Results

APPENDIX B: ERROR PROPOGATION AND UNCERTAINTY

Uncertainty values for measured quantities including void fraction, bubble speed, and bubble size as resulting from both HFA and High-Speed video analysis were found via repeatability tests under multiple conditions using a pooled standard deviation with relative standard deviation also reported. This is the method applied by [32] and [33], for which similar conclusions for HFA local void fraction were found as to that shown here. The summary of the results can be seen in Table 3, with in-depth details found below.

$$s_p^2 = \frac{\sum_{i=1}^k ((n_i - 1) s_i^2)}{\sum_{i=1}^k (n_i - 1)}$$

Equation 3: Pool Standard Deviation (k=number of sets, n=number of samples in set)

Table 3: HFA and Camera Uncertainty Analysis

		Std Dev	%
HFA	Local VF	0.00877	10.63
	Ave. Diam. (mm)	0.18189	6.40
	Ave. Vel. (m/s)	0.01569	4.84
Camera	Ave. VF	0.00912	12.77
	Local VF	0.02584	21.02
	Ave. Diam. (mm)	0.28627	7.72
	Ave. Vel. (m/s)	0.01804	4.99

Local Void Fraction - HFA						STD DEV	N
T-30	T-50						
0.06039	0.06478					0.00310	2
T-29	T-33	T-34	T-35	T-36			
0.06335	0.0874	0.074	0.07554	0.0807		0.00891	4
T-31	T-43	T-63					
0.09943	0.1155	0.116				0.00946	3
T-32	T-37						
0.06917	0.08					0.01058	2
			Pooled	%			

			SD				
			0.00877	10.63			

Average Bubble Diameter (mm) - HFA						STD DEV	N
T-30	T-50						
2.144	2.361					0.15344	2
T-29	T-33	T-34	T-35	T-36			
2.808	2.735	3.065	2.937	2.822		0.12926	4
T-31	T-43	T-63					
2.96	3.44	3.443				0.27800	3
T-32	T-37						
2.664	2.746					0.05798	2
			Pooled SD	%			
			0.18189	6.40			

Average Bubble Velocity (m/s) - HFA						STD DEV	N
T-30	T-50						
0.267	0.299					0.02263	2
T-29	T-33	T-34	T-35	T-36			
0.3175	0.308	0.339	0.32	0.308		0.01269	4
T-31	T-43	T-63					
0.339	0.363	0.3767				0.01908	3
T-32	T-37						
0.328	0.328					0.00000	2
			Pooled SD	%			
			0.01569	4.84			

Average Void Fraction - Camera				STD DEV	N
T-30	T-50				
0.0361	0.0403			0.0029698	2

T-31	T-43	T-63			
0.0809	0.1006	0.0991		0.0109665	3
		Pooled SD	%		
		0.00912	12.77		

Local Void Fraction - Camera				STD DEV	N
T-30	T-50				
0.0827591	0.0649			0.0126283	2
T-31	T-43	T-63			
0.1207636	0.169956	0.176172		0.0303552	3
		Pooled SD	%		
		0.02584	21.02		

Average Bubble Diameter (mm) - Camera				STD DEV	N
T-30	T-50				
2.8610912	2.7448069			0.0822254	2
T-29	T-33	T-34			
3.9613483	4.653	4.3261394		0.3457539	3
		Pooled SD	%		
		0.28627	7.72		

Average Bubble Velocity (m/s) - Camera				STD DEV	N
T-30	T-50				
0.3684929	0.3504571			0.0127532	2
T-31	T-43	T-63			
0.3458143	0.3576929	0.3851389		0.0201693	3
		Pooled SD	%		
		0.01804	4.99		

APPENDIX C: HFA SIGNAL ANALYSIS CODE

Pure Slope Phase Discrimination and Void Fraction Calculation Code

```
% Input Test Parameters
BlockS=131072; %Block Size
freq=10000; %Sampling Frequency
nBlock=84; %Total Number of Blocks Recorded (whole test)
nPoints=11; %Number of Locations Examined in Channel
C=7; %Number of Blocks Sampled Per Location in Channel
K=C*BlockS; %Total Number of Points in Each Location Sample
dthresh=36; %Primary Slope Threshold
dthresh2=5; %Secondary Slope Threshold
dthresh3=10; %Buffer Slope Value

% Loads Files
M=zeros(BlockS,nBlock);
for i=1:nBlock
    if i<10
        filename=['AW-TEST-T-42/AW-TEST-T-42.B000',int2str(i)];
    elseif i>=10 && i<100
        filename=['AW-TEST-T-42/AW-TEST-T-42.B00',int2str(i)];
    else
        filename=['AW-TEST-T-42/AW-TEST-T-42.B0',int2str(i)];
    end
    Tempdata=dlmread(filename);
    M(:,i)=Tempdata(:,3);
end
disp('Files Read')

% Builds voltage vectors
V=zeros(K,nPoints);
for m=1:nPoints
    z=C*(m-1);
    V(:,m)=[M(:,1+z);M(:,2+z);M(:,3+z);M(:,4+z);M(:,5+z);M(:,6+z);M(:,7+z)];
end
% Builds time vector
t=zeros(K,1);
for i=1:K
    t(i)=(i-1)/freq;
end
% Takes first derivative of voltage data
dV=zeros(K,nPoints);
for m=1:nPoints;
    for i=2:K-1
        dV(i,m)=(V(i+1,m)-V(i-1,m))/(t(i+1)-t(i-1));
    end
end
disp('Vectors Created')

for m=1:nPoints
% Use pure slope (lead and trail) thresh to calculate void fraction
    dV(1,m)=dthresh3;
```



```

dV(2,m)=-dthresh3;
dV(3,m)=dthresh3;
Phase=zeros(K,1);
b=0;
water=1;
air=0;
bub=0;

% LEAD PORTION - Look for front interfaces
for i=1:K
    if bub==0
        if dV(i,m)<=-dthresh
            Phase(i)=air;
            bub=1;
        else
            Phase(i)=water;
        end
    else
        if dV(i,m)>=dthresh2
            Phase(i)=water;
            bub=0;
        else
            Phase(i)=air;
        end
    end
end
% TRAIL PORTION - Look for rear interfaces
for i=1:K
    if dV(i,m)>=dthresh
        j=i;
        while dV(j,m)>=-dthresh2
            j=j-1;
        end
        while dV(j,m)<=dthresh2
            Phase(j)=air;
            j=j-1;
        end
    end
end
%Track Air Phase
for i=1:K
    if Phase(i)==air
        b=b+1;
    end
end
%Void Fractions
VF(m)=b/K;
end

```

Hybrid (Amplitude Trigger) Phase Discrimination and Void Fraction Calculation Code

```

% Input Test Parameters
BlockS=131072; %Block Size

```

```

freq=10000; %Sampling Frequency
nBlock=77; %Total Number of Blocks Recorded (whole test)
nPoints=11; %Number of Locations Examined in Channel
C=7; %Number of Blocks Sampled Per Location in Channel
K=C*BlockS; %Total Number of Points in Each Location Sample
dthresh=36; %Primary Slope Threshold
dthresh2=5; %Secondary Slope Threshold
dthresh3=10; %Buffer Slope Value

% Loads Files
M1=zeros(BlockS,nBlock);
for i=1:nBlock
    if i<10
        filename=['AW-TEST-T-65/AW-TEST-T-65.B000',int2str(i)];
    elseif i>=10 && i<100
        filename=['AW-TEST-T-65/AW-TEST-T-65.B00',int2str(i)];
    else
        filename=['AW-TEST-T-65/AW-TEST-T-65.B0',int2str(i)];
    end
    Tempdata = dlmread(filename);
    M(:,i)=Tempdata(:,3);
end
clear Tempdata
disp('Files Read')

%Builds voltage vectors
V=zeros(K,nPoints);
for m=1:nPoints
    z=C*(m-1);
    V(:,m)=[M(:,1+z);M(:,2+z);M(:,3+z);M(:,4+z);M(:,5+z);M(:,6+z);M(:,7+z)];
end
clear M*
%Builds time vector
t=zeros(K,1);
for i=1:K
    t(i)=(i-1)/freq;
end
%Takes first derivative of voltage data
dV=zeros(K,nPoints);
for m=1:nPoints;
    for i=2:K-1
        dV(i,m)=(V(i+1,m)-V(i-1,m))/(t(i+1)-t(i-1));
    end
end
disp('Vectors Created')

for m=1:nPoints
    %Use hybrid technique to calculate void fraction
    Phase=zeros(K,1);
    water=1;
    air=0;
    n=400;
    thresh=zeros(n+1,1);
    VF=zeros(n+1,1);

```

```

for s=1:n+1
    a=0;
    thresh(s)=max(V(:,m))-(1/n)*(s-1)*(max(V(:,m))-min(V(:,m)));
    for i=2:K
        Phase(i)=water;
        if V(i,m)<thresh(s) && V(i-1,m)>thresh(s)
            j=i;
            while dV(j,m)<-dthresh2
                Phase(j)=air;
                j=j-1;
            end
        elseif V(i,m)<thresh(s)
            Phase(i)=air;
        elseif V(i,m)>thresh(s) && V(i-1,m)<thresh(s)
            j=i;
            while dV(j,m)>dthresh2
                Phase(j)=water;
                j=j-1;
            end
        end
    end
    for i=1:K
        if Phase(i)==air
            a=a+1;
        end
    end
    VF(s)=a/K;
end
VF
end

```

Bubble Velocity Cross Correlation Code

```

% Input Test Parameters
BlockS=131072; %Block Size
freq=10000; %Sampling Frequency
nBlock=77; %Total Number of Blocks Recorded (whole test)
nPoints=11; %Number of Locations Examined in Channel
C=7; %Number of Blocks Sampled Per Location in Channel
K=C*BlockS; %Total Number of Points in Each Location Sample
dthresh=36; %Primary Slope Threshold
dthresh2=5; %Secondary Slope Threshold
dthresh3=10; %Buffer Slope Value

% Loads Files
M1=zeros(BlockS,nBlock);
M2=zeros(BlockS,nBlock);
for i=1:nBlock
    if i<10
        filename=['AW-TEST-T-65/AW-TEST-T-65.B000',int2str(i)];
    elseif i>=10 && i<100
        filename=['AW-TEST-T-65/AW-TEST-T-65.B00',int2str(i)];
    else

```

```

        filename=['AW-TEST-T-65/AW-TEST-T-65.B0',int2str(i)];
    end
    Tempdata = dlmread(filename);
    M1(:,i)=Tempdata(:,3);
    M2(:,i)=Tempdata(:,2);
end
clear Tempdata
disp('Files Read')

% Builds voltage vectors
V=zeros(K,nPoints);
Vb=zeros(K,nPoints);
for m=1:nPoints
    z=C*(m-1);
    V(:,m)=[M1(:,1+z);M1(:,2+z);M1(:,3+z);M1(:,4+z);M1(:,5+z);M1(:,6+z);
            M1(:,7+z)];
    Vb(:,m)=[M2(:,1+z);M2(:,2+z);M2(:,3+z);M2(:,4+z);M2(:,5+z);M2(:,6+z);
            M2(:,7+z)];
end
clear M*
% Builds time vector
t=zeros(K,1);
for i=1:K
    t(i)=(i-1)/freq;
end
% Takes first derivative of voltage data
dV=zeros(K,nPoints);
dVb=zeros(K,nPoints);
for m=1:nPoints;
    for i=2:K-1
        dV(i,m)=(V(i+1,m)-V(i-1,m))/(t(i+1)-t(i-1));
        dVb(i,m)=(Vb(i+1,m)-Vb(i-1,m))/(t(i+1)-t(i-1));
    end
end
disp('Vectors Created')

for m=1:nPoints
    water=1;
    air=0;
    n=40;
    for s=1:n+1
        %Phase discrimination (hybrid) first sensor
        Phase=zeros(K,1);
        if s<=n/2 %Thresh limits from void fraction code
            thresh(s)=1.271+(4/n)*(s-1)*(1.379-1.271);
        else
            thresh(s)=1.379;
        end
        a=0;
        for i=2:K
            Phase(i)=water;
            if V(i,m)<thresh(s) && V(i-1,m)>thresh(s)
                j=i;
            end
        end
    end
end

```

```

        while dV(j,m)<-dthresh2
            Phase(j)=air;
            j=j-1;
        end
    elseif V(i,m)<thresh(s)
        Phase(i)=air;
    elseif V(i,m)>thresh(s) && V(i-1,m)<thresh(s)
        j=i;
        while dV(j,m)>dthresh2
            Phase(j)=water;
            j=j-1;
        end
    end
end
end
for i=1:K
    if Phase(i)==air
        a=a+1;
    end
end
VF(s)=a/K;

%Phase discrimination (hybrid) second sensor
Phaseb=zeros(K,1);
if s>=n/2+1 %Thresh limits from void fraction code
    threshb(s)=2.215+(4/n)*((s-n/2)-1)*(2.611-2.215);
else
    threshb(s)=2.611;
end
b=0;
for i=2:K
    Phaseb(i)=water;
    if Vb(i,m)<threshb(s) && Vb(i-1,m)>threshb(s)
        j=i;
        while dVb(j,m)<-dthresh2
            Phaseb(j)=air;
            j=j-1;
        end
    elseif Vb(i,m)<threshb(s)
        Phaseb(i)=air;
    elseif Vb(i,m)>threshb(s) && Vb(i-1,m)<threshb(s)
        j=i;
        while dVb(j,m)>dthresh2
            Phaseb(j)=water;
            j=j-1;
        end
    end
end
end
for i=1:K
    if Phaseb(i)==air
        b=b+1;
    end
end
VFb(s)=b/K;

```

```

%Cross Correlation
K1=length(Phase);
range=200;
Prod=zeros(K1-2*range,1);
R=zeros(2*range+1,1);
tau=zeros(2*range+1,1);
for i=-range:range
    for j=range+1:K1-range
        Prod(j)=(Phase(j))*(Phaseb(j+i)).0001;
    end
    R(i+range+1)=sum(Prod)/t(K1);
    tau(i+range+1)=i*.0001;
end
[C,I]=max(R);
tau2(s,m)=tau(I)
end
figure,plot3(thresh,threshb,tau2(:,m))
end

```

Chord Length Distribution and Average Diameter Code

```

% Input Test Parameters
BlockS=131072; %Block Size
freq=10000; %Sampling Frequency
nBlock=77; %Total Number of Blocks Recorded (whole test)
nPoints=11; %Number of Locations Examined in Channel
C=7; %Number of Blocks Sampled Per Location in Channel
K=C*BlockS; %Total Number of Points in Each Location Sample
dthresh=36; %Primary Slope Threshold
dthresh2=5; %Secondary Slope Threshold
dthresh3=10; %Buffer Slope Value

% Loads Files
M1=zeros(BlockS,nBlock);
for i=1:nBlock
    if i<10
        filename=['AW-TEST-T-65/AW-TEST-T-65.B000',int2str(i)];
    elseif i>=10 && i<100
        filename=['AW-TEST-T-65/AW-TEST-T-65.B00',int2str(i)];
    else
        filename=['AW-TEST-T-65/AW-TEST-T-65.B0',int2str(i)];
    end
    Tempdata = dlmread(filename);
    M(:,i)=Tempdata(:,3);
end
clear Tempdata
disp('Files Read')

% Builds voltage vectors

```

```

V=zeros(K,nPoints);
for m=1:nPoints
    z=C*(m-1);
    V(:,m)=[M(:,1+z);M(:,2+z);M(:,3+z);M(:,4+z);M(:,5+z);M(:,6+z);M(:,7+z)];
end
clear M*
% Builds time vector
t=zeros(K,1);
for i=1:K
    t(i)=(i-1)/freq;
end
% Takes first derivative of voltage data
dV=zeros(K,nPoints);
for m=1:nPoints;
    for i=2:K-1
        dV(i,m)=(V(i+1,m)-V(i-1,m))/(t(i+1)-t(i-1));
    end
end
disp('Vectors Created')

for m=1:nPoints
    n=400;
    thresh=zeros(n+1,nPoints);
    VF=zeros(n+1,nPoints);
    for s=1:n+1
        thresh(s,m)=max(V(:,m))-(1/n)*(s-1)*(max(V(:,m))-min(V(:,m)));
    end
    %Use hybrid technique to calculate void fraction
    water=1;
    air=0;
    ST=size(thresh);
    Phase=zeros(K,1);
    Chord=zeros(100,ST(1));
    for s=1:ST(1)
        a=0;
        for i=2:K
            Phase(i)=water;
            if V(i,m)<thresh(s,m) && V(i-1,m)>thresh(s,m)
                j=i;
                while dV(j,m)<-dthresh2
                    Phase(j)=air;
                    j=j-1;
                end
            elseif V(i,m)<thresh(s,m)
                Phase(i)=air;
            elseif V(i,m)>thresh(s,m) && V(i-1,m)<thresh(s,m)
                j=i;
                while dV(j,m)>dthresh2
                    Phase(j)=water;
                    j=j-1;
                end
            end
        end
    end
end
end

```

```

    for i=1:K
        if Phase(i)==air
            a=a+1;
        end
    end
    VF(s,m)=a/K;

    %Extracts Chord Length
    L=0;
    j=1;
    for i=2:K
        if Phase(i)==air
            L=L+1;
            Chord(j,s)=L+1;
        else
            L=0;
        end
        if Phase(i)==water && Phase(i-1)==air
            ChordLoc(j,s)=t(i-1);
            j=j+1;
        end
    end
end

BL=zeros(m,ST(1));
%Calculates bubble size and speed
delta=1.016; %Distance between sensors (mm)
Vel=delta/tau(m); %Interfacial bubble velocity (mm/s)
Bub=.0001*Chord*Vel;
for s=1:ST(1)
    edges=0:1:max(Chord(:,s));
    edges(1)=.001;
    hista=histc(Chord(:,s),edges);
    [A,IX]=sort(hista,'descend');
    sum=0;
    freq=0;
    for i=1:max(edges)
        freq=hista(i)*edges(i)+freq;
        sum=hista(i)+sum;
    end
    freq;
    sum;
    rt=.0001*freq/sum; %average bubble residence time (s)
    BL(s,m)=rt*Vel; %average bubble length (mm)
end
end
end

```


LIST OF REFERENCES

- [1] R. Kumar, C. C. Maneri, and T. D. Strayer, "Modeling and Numerical Prediction of Flow Boiling in a Thin Geometry," *Journal of Heat Transfer*, vol. 126, p. 22, 2004.
- [2] R. Kumar, T. A. Trabold, and C. C. Maneri, "Experiments and Modeling in Bubbly Flows at Elevated Pressures," *Journal of Fluids Engineering*, vol. 125, pp. 469-478, 2003.
- [3] R. Kumar, M. Gottmann, and K. R. Sridhar, "Film thickness and wave velocity measurements in a vertical duct," *Journal of Fluids Engineering*, vol. 124, p. 634, 2002.
- [4] R. Kumar and T. A. Trabold, "High Pressure Annular Two Phase Flow in a Narrow Duct: Part II--Three Field Modeling," *Journal of Fluids Engineering*, vol. 122, pp. 375-383, 2000.
- [5] R. Kumar and T. A. Trabold, "Effect of Pressure With Wall Heating in Annular Two-Phase Flow," *Journal of Fluids Engineering*, vol. 125, p. 84, 2003.
- [6] T. Wilmarth and M. Ishii, "Two-phase flow regimes in narrow rectangular vertical and horizontal channels," *International Journal of Heat and Mass Transfer*, vol. 37, pp. 1749-1758, 1994.
- [7] P. F. Vassallo and R. Kumar, "Liquid and gas velocity measurements using LDV in air-water duct flow," *Experimental Thermal and Fluid Science*, vol. 19, pp. 85-92, 1999.
- [8] G. J. Kirouac, T. A. Trabold, P. F. Vassallo, W. E. Moore, and R. Kumar, "Instrumentation development in two-phase flow," *Experimental Thermal and Fluid Science*, vol. 20, pp. 79-93, 1999.
- [9] G. Comte-Bellot and J. F. Foss, "Thermal Anemometry," in *Springer Handbook of Experimental Fluid Mechanics*, C. Tropea, A. L. Yarin, and J. F. Foss, Eds. New York: Springer-Verlag, 2007, pp. 229-287.
- [10] "IFA 300 Constant Temperature Anemometer System Operation Manual," Revision C ed Shoreview, MN: TSI Inc., 2007.
- [11] R. H. S. Winterton and J. S. Munaweera, "Bubble size in two-phase gas-liquid bubbly flow in ducts," *Chemical Engineering and Processing*, vol. 40, pp. 437-447, 2001.

- [12] K. Mishima, T. Hibikia, and H. Nishiharaa, "Some Characteristics of Gas-Liquid Flow in Narrow Rectangular Ducts," *International Journal of Multiphase Flow*, vol. 19, pp. 115-124, 1993.
- [13] O. C. Jones, Jr. and N. Zuber, "Slug-annular transition with particular reference to narrow rectangular ducts.," in *Two-Phase Momentum, Heat and Mass Transfer in Chemical, Process and Energy Engineering Systems*. vol. 1, F. Durst, G. V. Tsiklauri, and N. H. Afgan, Eds. Washington DC: Hemisphere, 1979, pp. 345-355.
- [14] M. Ishii, "One-Dimensional Drift Flux Model and Constitutive Equations for Relative Motion Between Phases in Various Two-Phase Flow Regimes," in *ANL Report*. vol. ANL-77-47, 1977.
- [15] J. L. Xu, P. Cheng, and T. S. Zhao, "Gas-liquid two-phase flow regimes in rectangular channels with mini/micro gaps," *International Journal of Multiphase Flow*, vol. 25, pp. 411-432, 1999.
- [16] T. Hibiki and K. Mishima, "Flow regime transition criteria for upward two-phase flow in vertical narrow rectangular channels," *Nuclear Engineering and Design*, vol. 203, pp. 117-131, 2001.
- [17] K. Bremhorst and D. B. Gilmore, "Response of Hot Wire Anemometer Probes to A Stream of Air Bubbles in a Water Flow," *Journal of Physics E: Scientific Instruments*, vol. 9, pp. 347-352, 1976.
- [18] B. Farrar, A. L. Samways, J. Ali, and H. H. Bruun, "A Computer-Based Hot-Film Technique for Two-Phase Flow Measurements," *Measurement Science and Technology*, vol. 6, pp. 1528-1537, 1995.
- [19] B. Farrar and H. H. Bruun, "Interaction Effects Between a Cylindrical Hot-Film Anemometer Probe and Bubbles in Air/Water and Oil/Water Flows," *Journal of Physics E: Scientific Instruments*, vol. 22, p. 114, 1989.
- [20] J. Rensen, S. Luther, J. de Vries, and D. Lohse, "Hot-Film Anemometry in Bubbly Flow I: Bubble-Probe Interaction," *International Journal of Multiphase Flow*, vol. 31, pp. 285-301, 2005.
- [21] H. Toral, "A Study of the Hot Wire Anemometer for Measuring Void Fraction in Two Phase Flow," *Journal of Physics E: Scientific Instruments*, vol. 14, pp. 882-827, 1981.
- [22] T. A. Trabold, W. E. Moore, and W. O. Morris, "Hot-Film Anemometer Measurements in Adiabatic Two-Phase Refrigerant Flow through a Vertical Duct," in *ASME Fluids Engineering Division Summer Meeting*, Vancouver, B.C., 1997.

- [23] F. Resch, H. Leutheusser, and S. Alemu, "Bubbly Two-Phase Flow in Hydraulic Jump," *Journal of the Hydraulics Division*, vol. 100, pp. 137-149, 1974.
- [24] T. A. Trabold and R. Kumar, "High Pressure Annular Two Phase Flow in a Narrow Duct: Part I--Local Measurements in the Droplet Field," *Journal of Fluids Engineering*, vol. 122, pp. 364-374, 2000.
- [25] N. T. Thang and M. R. Davis, "The Structure of Bubbly Flow through Venturis," *International Journal of Multiphase Flow*, vol. 5, pp. 17-37, 1979.
- [26] R. van der Welle, "Void Fraction, Bubble Velocity and Bubble Size in Two-Phase Flow," *International Journal of Multiphase Flow*, vol. 11, pp. 317-345, 1985/6// 1985.
- [27] G. Wang and C. Y. Ching, "Measurement of Multiple Gas-Bubble Velocities in Gas-Liquid Flows Using Hot-Film Anemometry," *Experiments in Fluids*, vol. 31, pp. 428-439, 2001.
- [28] P. F. Vassallo, T. A. Trabold, R. Kumar, and D. M. Considine, "Slug-to-annular regime transitions in R-134a flowing through a vertical duct," *International Journal of Multiphase Flow*, vol. 27, pp. 119-145, 2001.
- [29] J. Canny, "A Computational Approach to Edge Detection," *IEEE Transactions on Pattern Analysis and Machine Intelligence*, vol. 8, pp. 679-698, 1986.
- [30] W. Liu and N. N. Clark, "Relationships between distributions of chord lengths and distributions of bubble sizes including their statistical parameters," *International Journal of Multiphase Flow*, vol. 21, pp. 1073-1089, 1995.
- [31] W. Liu, N. N. Clark, and A. I. Karamavruc, "Relationships between bubble size distributions and chord-length distribution in heterogeneously bubbling systems," *Chemical Engineering Science*, vol. 53, pp. 1267-1276, 1998.
- [32] T. A. Trabold and R. Kumar, "Vapor core turbulence in annular two-phase flow," *Experiments in Fluids*, vol. 28, pp. 187-194, 2000.
- [33] T. A. Trabold, R. Kumar, and P. F. Vassallo, "Experimental study of dispersed droplets in high-pressure annular flows," *Journal of Heat Transfer*, vol. 121, pp. 924-933, 1999.